

The First Dedicated Survey of Atmospheric Escape from Planets Orbiting F Stars

MORGAN SAIDEL ,¹ SHREYAS VISSAPRAGADA ,² HEATHER A. KNUTSON ,¹ ETHAN SCHREYER ,³
 MICHAEL GREKLEK-MCKEON ,⁴ JONATHAN GOMEZ BARRIENTOS ,¹ W. GARRETT LEVINE ,^{5,6} CARLOS GASCÓN ,^{7,8}
 MORGAN MACLEOD ,⁷ HAEDAM IM ,⁹ AND NICK TUSAY ,¹⁰

¹Division of Geological and Planetary Sciences, California Institute of Technology, Pasadena, CA 91125, USA

²Carnegie Science Observatories, 813 Santa Barbara Street, Pasadena, CA 91101, USA

³Department of Astronomy and Astrophysics, University of California, Santa Cruz, CA 95064, USA

⁴Earth and Planets Laboratory, Carnegie Institution for Science, Washington, DC 20015, USA

⁵Department of Earth, Planetary, and Space Sciences, University of California, Los Angeles, CA 90095, USA

⁶Department of Astronomy, Yale University, New Haven, CT, 06511, USA

⁷Center for Astrophysics, Harvard & Smithsonian, 60 Garden Street, MS-16, Cambridge, MA 02138, USA

⁸Institut d'Estudis Espacials de Catalunya (IEEC), 08860 Castelldefels, Barcelona, Spain

⁹Department of Physics, Massachusetts Institute of Technology, Cambridge, MA 02139, USA

¹⁰Department of Astronomy, University of Washington, 3910 15th Avenue NE, Seattle, WA 98195, USA

ABSTRACT

Hydrodynamic escape can strip the envelopes of close-in exoplanets, but most observations of atmospheric mass loss to date have been confined to planets orbiting K and M dwarfs. A growing body of detections of atmospheric escape from planets orbiting early-type stars indicates that they may have significantly stronger and more extended outflows than planets orbiting cooler stars. However, it is unclear whether this limited sample of planets is representative of all gas giants orbiting early-type stars. Motivated by this question, we initiated the first dedicated survey of atmospheric escape from gas giants orbiting F stars in order to understand how their distinct radiation environments shape planetary outflows. We observed ten transits of six planets in an ultra-narrowband filter centered on the metastable helium line using Palomar/WIRC. We report strong ($> 3\sigma$) detections of atmospheric escape for WASP-12 b and WASP-180 A b, tentative ($> 2\sigma$) detections for WASP-93 b and HAT-P-8 b, and non-detections for WASP-103 b and KELT-7 b. We fit these measurements with a 1D Parker wind model to derive corresponding mass-loss rates, and combine our results with literature measurements to obtain an updated picture of mass loss from planets orbiting early-type stars. Our results indicate that the observed variation in mass-loss rates can be explained by a combination of Roche filling factor and XUV luminosity, and disfavors NUV-driven escape models.

1. INTRODUCTION

Exoplanets on close-in orbits are exposed to intense irradiation from their host stars, powering mass loss that can catastrophically alter their evolution. Mass loss is thought to play a central role in sculpting the population of close-in exoplanets, and is likely responsible for the creation of both the ‘evaporation valley’ (a period-dependent separation between rocky super-Earths and sub-Neptunes; e.g., B. J. Fulton et al. 2017; J. G. Rogers et al. 2024) and the lower boundary of the ‘Neptune desert’ (a deficit of Neptune-sized planets on close-in orbits; e.g., J. E. Owen & D. Lai 2018). To quantify

the effect of atmospheric mass loss on the population of close-in planets, we must be able to accurately predict mass-loss rates for a wide range of stellar environments. By measuring the amount of absorption in strong atomic lines including Ly α , H α , and the 1083 nm line of metastable helium (He *) when the planet passes in front of its host star, we can detect atmospheric outflows from close-in transiting planets and characterize their corresponding mass-loss rates, outflow geometries, and kinematics (see reviews by J. E. Owen 2019; L. A. Dos Santos 2023). This in turn allows us to test predictions from current mass-loss models, and guide the development of a new generation of improved models.

To date, there have been more than 25 published detections ($> 3\sigma$) of atmospheric escape using Ly α , H α , and He * (for a recent list, see the review by E. M. R.

Kempton & H. A. Knutson 2024). Unlike Ly α , which can only be observed from space and suffers from interstellar medium absorption in the line core, He* and H α are easily accessible from the ground. H α requires a significant population of excited hydrogen, and as a result the small number of H α detections that have been published to date are limited to the subset of planets with the highest XUV fluxes, many of which orbit early-type stars (e.g., A. G. Jensen et al. 2012; F. Yan & T. Henning 2018; N. Casasayas-Barris et al. 2019; A. Wytenbach et al. 2020; S. Czesla et al. 2022; D. Yan et al. 2021, 2022).

In contrast, He* acts as a strong tracer of atmospheric outflows over a relatively broad range of temperatures and mass loss rates (A. Oklopčić & C. M. Hirata 2018). This has made He* the most successful method for detecting atmospheric outflows, with over 20 published detections to date (see Figure 1). Most of these detections have been for planets orbiting K dwarfs, likely because He* is populated by extreme ultra-violet (EUV) radiation and depopulated by mid-ultra-violet (mid-UV) radiation, and K dwarfs provide the optimal radiation balance (A. Oklopčić & C. M. Hirata 2018; A. Oklopčić 2019). However, an ever-growing list of He* detections for planets orbiting F stars (HAT-P-32 b, HAT-P-67 b, WASP-76 b, WASP-94 A b, WASP-121 b; S. Czesla et al. 2022; Z. Zhang et al. 2023; A. Bello-Arufe et al. 2023; M. Gully-Santiago et al. 2024; S. Czesla et al. 2024b; S. Mukherjee et al. 2025; J. Orell-Miquel et al. 2025) indicates that hotter stars can also be suitable targets for mass loss studies using this feature. For planets whose outflows are also detectable in H α , simultaneous measurements of the excess absorption in both H α and He* can be used to directly constrain the H/He ratio of the outflow (e.g., D. Yan et al. 2022; S. Czesla et al. 2022; D. Yan et al. 2024).

There are currently six planets orbiting F or A stars with published mass loss rates derived from He*, H α , or a combination of the two. Four of these planets (HAT-P-32 b, HAT-P-67 b, KELT-9 b, and WASP-121 b) exhibit unusually high mass-loss rates ($>10^{12}$ g s $^{-1}$), and two (HAT-P-32 b and HAT-P-67 b) have very spatially extended outflows ($> 50 \times$ the planet radius; Z. Zhang et al. 2023; M. Gully-Santiago et al. 2024; S. Czesla et al. 2024b). The reported mass loss rate for WASP-33 b is also just barely below this threshold (D. Yan et al. 2021). In contrast, WASP-94 A b appears to have a more typical mass loss rate of 7×10^{10} g s $^{-1}$ (S. Mukherjee et al. 2025), and K. A. Bennett et al. (2023) reported a 3σ upper bound on the mass-loss rate of WASP-48 b of 2.5×10^{11} g s $^{-1}$. WASP-48 is an old (~ 7.9 Gyr) slightly evolved F star and will have a lower XUV flux than

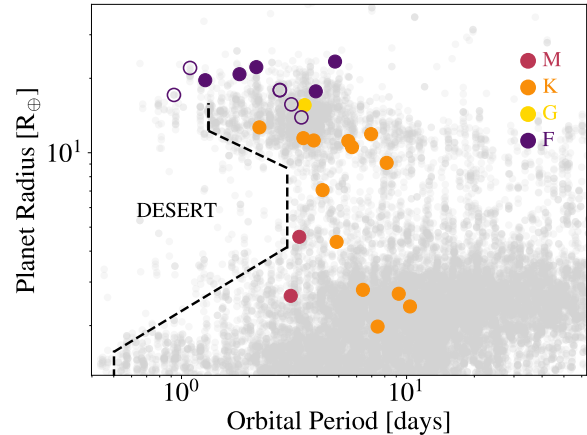


Figure 1. Confirmed transiting planet radii and periods drawn from the NASA Exoplanet Archive on August 26th, 2025 (R. L. Akeson et al. 2013; NASA Exoplanet Archive 2024). Closed colored circles represent He* detections of atmospheric escape as a function of spectral type. Open circles denote survey targets. The dashed lines indicate the Neptune desert boundary from A. Castro-González et al. (2024).

younger, less evolved stars of the same spectral type, likely contributing to the non-detection and low upper bound on the mass loss rate reported in K. A. Bennett et al. (2023). WASP-76 b does not currently have a reported mass-loss rate for its He* absorption signal (J. Orell-Miquel et al. 2025).

Given this limited sample size, it is unclear whether the strong outflows from HAT-P-32 b, HAT-P-67 b, KELT-9 b, WASP-33 b, and WASP-121 b are broadly representative of most gas giants orbiting early-type stars, or if they instead reflect characteristics particular to these systems. For example, most of these planets fill 40 – 50% of their Roche lobes (“Roche filling factor”), making them particularly susceptible to enhanced atmospheric loss via Roche lobe overflow (RLO; e.g., B. Jackson et al. 2017; T. T. Koskinen et al. 2022).

Alternatively, the planets with the highest measured mass loss rates might have enhanced X-ray and EUV luminosities that could drive increased mass loss. This is supported by *XMM-Newton* observations of HAT-P-32 and WASP-121, which revealed X-ray (5–100 Å) luminosities of 2.3×10^{29} erg s $^{-1}$ (S. Czesla et al. 2022) and 1.3×10^{29} erg s $^{-1}$ (S. Czesla et al. 2024b), respectively. However, KELT-9 has an upper bound of 3×10^{29} erg s $^{-1}$ (J. Sanz-Forcada et al. 2025), and there are currently no published X-ray or EUV constraints for HAT-P-67, WASP-33, or WASP-94 A.

Lastly, it is also possible that the high NUV luminosities of early-type stars might contribute additional power that could drive massive outflows. A. García

Muñoz & P. C. Schneider (2019) found that the high NUV fluxes of these stars can lead to Balmer-driven escape, resulting in atmospheric mass-loss rates as much as two orders of magnitude larger than the corresponding rates from EUV and X-ray emission alone. If correct, this would suggest that gas giants orbiting early-type stars with high NUV fluxes should experience systematically higher atmospheric mass-loss rates than their counterparts around cooler stars.

In order to quantify the importance of these various factors in determining mass-loss rates for planets orbiting early-type stars, we require additional detections of atmospheric mass loss. With this goal in mind, we designed a dedicated ground-based survey to search for atmospheric escape from six gas giants orbiting F stars: HAT-P-8, WASP-93, WASP-180 A, WASP-103, KELT-7, and WASP-12. These systems have varying Roche filling factors, projected stellar rotational velocities ($vsini_*$; see Table 1), EUV and NUV fluxes, allowing us to explore the importance of these parameters for determining the outflow properties. In Section 2 we detail our target selection, observational setup and data reduction process. We detail the results of our observational survey in Section 3 and retrieve mass-loss rates based on these results in Section 4. We discuss the implication of our results on the broader landscape of atmospheric escape observations in Section 5. Finally, we summarize our conclusions in Section 6.

2. OBSERVATIONS & DATA REDUCTION

2.1. Target Selection

We selected targets for our survey using the NASA Exoplanet Archive (R. L. Akeson et al. 2013; J. L. Christiansen et al. 2025). We identified an initial sample of transiting gas giant planets ($R > 4 R_\oplus$) orbiting bright ($J < 12$) F stars ($T_{\text{eff}} = 6000 - 7935$ K) that are accessible from Palomar Observatory (declinations $> -20^\circ$). For each planet, we then calculated a predicted mass-loss rate using an energy-limited mass-loss equation (A. Caldrioli et al. 2022). We fixed the heating efficiency η to 0.40, as A. Caldrioli et al. (2022) notes that most heating efficiencies for thermal escape are between 0.3 to 1. While high gravity planets can have lower efficiencies than 0.3, many of our targets have high Roche filling factors, meaning the atmospheres of these planets should therefore not be in a high gravity regime. We conservatively assumed a solar EUV spectrum (L. A. Dos Santos et al. 2022) scaled by $(R_\star/R_\odot)^2$ for every star in the sample, as there are relatively few measurements of EUV spectra for stars in this temperature range. For all planets, we estimated a thermosphere temperature (T_0) of the outflow based on the planet's

orbital period following M. Salz et al. (2016): $P \geq 4$ days: $T_0 = 6000$ K; $1 \leq P \leq 4$ days: $T_0 = 8000$ K; $P \leq 1$ days: $T_0 = 10,000$ K). We combined these thermosphere temperatures and mass-loss rates to calculate the predicted He^* absorption signals during transit using the open-source `p-winds` package (L. A. Dos Santos et al. 2022), which models escaping planetary atmospheres as one-dimensional hydrodynamic Parker winds. We then integrated the predicted He^* excess absorption spectrum for each planet over the transmission of the Palomar/WIRC He^* filter using Eqn. 3 in S. Vissapragada et al. (2020b) to obtain a predicted mid-transit excess absorption value (i.e., the difference between the expected transit depths for a planet with and without an atmospheric outflow). Lastly, we calculated the expected photometric noise and corresponding SNR for a detection of excess absorption during transit by scaling the photometric noise from previous observations (e.g., S. Vissapragada et al. 2022; M. Saidel et al. 2025) to the J magnitudes of each stellar host. We rank-ordered our targets by SNR and selected the six highest SNR targets, additionally checking to ensure that our chosen sample spanned a range of $vsini_*$ ($2-70 \text{ km s}^{-1}$) and Roche filling factors ($0.20 - 0.55$). Our six survey targets are: HAT-P-8, WASP-93, WASP-180 A, WASP-103, KELT-7, and WASP-12. We note that our survey originally included another target with a high predicted SNR, KELT-17, but the weather on our scheduled nights for this target was poor and we were unable to obtain any usable observations.

2.2. Palomar/WIRC Data Collection & Reduction

We obtained a total of ten photometric transit observations for our six survey targets between 2023-2025, with twelve additional transit opportunities lost to poor weather. These observations used an ultra-narrowband helium filter (FWHM: 0.635 nm) centered on the 1083.3 nm He^* feature (S. Vissapragada et al. 2020b). We followed a similar procedure to that outlined in S. Vissapragada et al. (2020b); K. Paragas et al. (2021); S. Vissapragada et al. (2022); W. G. Levine et al. (2024); J. Pérez-González et al. (2024); M. Saidel et al. (2025), which we summarize briefly here. All observations began with a helium arc lamp calibration image, which allowed us to position each target on the detector location where the position-dependent transmission function was centered on the He^* line. Images were obtained using a custom-beam shaping diffuser which spreads incoming light into a top-hat shaped point-spread function (psf) with a FWHM of $3''$, improving the duty cycle of our observations and minimizing time-correlated systematics (G. Stefansson et al. 2017;

Table 1. Summary of target stellar and planetary properties.

Planet	R_p (R_J)	M_p (M_J)	R_\star (R_\odot)	M_\star (M_\odot)	T_{eff} (K)	$vsini_\star$ (km s^{-1})	R_p/R_{Roche}	λ ($^\circ$)	References
HAT-P-8 b	1.500 ± 0.070	1.354 ± 0.035	$1.580^{+0.080}_{-0.060}$	1.280 ± 0.040	6200 ± 80	11.50 ± 0.50	0.23	$-17^{+9.2}_{-11.5}$	L09, M11, B17
WASP-93 b	1.597 ± 0.077	1.47 ± 0.29	1.524 ± 0.040	1.334 ± 0.033	6700 ± 100	37 ± 3	0.27	-	H16
WASP-180 A b	1.24 ± 0.04	0.9 ± 0.1	1.19 ± 0.06	1.17 ± 0.01	6500 ± 150	19.9 ± 0.6	0.20	-157 ± 2	T19
WASP-103 b	$1.528^{+0.073}_{-0.047}$	1.39 ± 0.22	$1.436^{+0.052}_{-0.031}$	$1.220^{+0.039}_{-0.036}$	6110 ± 160	10.6 ± 0.9	0.51	3 ± 33	G14, A16
KELT-7 b	1.60 ± 0.06	1.28 ± 0.18	$1.732^{+0.043}_{-0.045}$	$1.535^{+0.066}_{-0.054}$	6789 ± 50	69.3 ± 0.2	0.26	-2.7 ± 0.6	B15, Z16, S17
WASP-12 b	$1.965^{+0.088}_{-0.087}$	1.465 ± 0.079	$1.690^{+0.019}_{-0.018}$	$1.325^{+0.026}_{-0.018}$	6265 ± 50	$1.66^{+0.8}_{-0.4}$	0.55	59^{+15}_{-20}	A12, CS19, L24
Literature Measurements									
HAT-P-32 b	1.980 ± 0.045	$0.68^{+0.11}_{-0.10}$	$1.367^{+0.031}_{-0.030}$	$1.132^{+0.051}_{-0.050}$	6207 ± 88	20.7 ± 0.5	0.42	85.0 ± 1.5	A12, B17, W19
HAT-P-67 b	$2.085^{+0.096}_{-0.071}$	$0.34^{+0.25}_{-0.19}$	$2.546^{+0.099}_{-0.084}$	$1.642^{+0.155}_{-0.072}$	6406^{+65}_{-61}	35.8 ± 1.1	0.38	$2.9^{+6.4}_{-4.9}$	Z17
KELT-9 b	1.783 ± 0.009	2.44 ± 0.70	2.178 ± 0.011	1.978 ± 0.023	9550^{+194}_{-132}	111.4 ± 1.3	0.34	-84.8 ± 1.4	G17, H19, S19
WASP-33 b	$1.679^{+0.019}_{-0.030}$	3.28 ± 0.73	1.444 ± 0.034	1.495 ± 0.031	7430 ± 100	90 ± 10	0.43	251.2 ± 1.0	CC10, T16
WASP-94 A b	$1.72^{+0.06}_{-0.05}$	$0.452^{+0.035}_{-0.032}$	$1.62^{+0.05}_{-0.04}$	1.45 ± 0.09	6153^{+75}_{-76}	4.2 ± 0.5	0.46	151^{+16}_{-23}	NV14
WASP-121 b	1.753 ± 0.036	1.157 ± 0.070	1.458 ± 0.030	$1.358^{+0.075}_{-0.084}$	6459 ± 140	$65 - 120^a$	0.50	$87.20^{+0.41}_{-0.45}$	D16, B20

^aThis star is seen nearly pole-on, so we instead quote the estimated equatorial velocity from B20.

NOTE— The lower part of the table lists system parameters for F or A star planets with published measurements of atmospheric escape rates from the literature as a point of comparison. We do not include WASP-76 b as there is no reported mass loss constraint for this He^{*} detection. Roche filling factor is a derived property and refers to the fraction of the Roche lobe filled by the planet radius. λ is the sky-projected obliquity, “ $_$ ” signifies an unknown quantity. In the references column, L09 refers to D. W. Latham et al. (2009), M11 is C. Moutou et al. (2011), B17 is A. S. Bonomo et al. (2017), H16 is K. L. Hay et al. (2016), T19 is L. Y. Temple et al. (2019), G14 is M. Gillon et al. (2014), A16 is B. C. Addison et al. (2016), B15 is A. Bieryla et al. (2015), Z16 is G. Zhou et al. (2016), S17 is K. G. Stassun et al. (2017), A12 is S. Albrecht et al. (2012), CS19 is A. Chakrabarty & S. Sengupta (2019), L24 is P. Leonardi et al. (2024) , W19 is Y. H. Wang et al. (2019), Z17 is G. Zhou et al. (2017), G17 is B. S. Gaudi et al. (2017), S17 is K. G. Stassun et al. (2017), H17 is H. J. Hoeijmakers et al. (2019), CC10 is A. Collier Cameron et al. (2010), T16 is J. D. Turner et al. (2016), NV14 is M. Neveu-VanMalle et al. (2014), D16 is L. Delrez et al. (2016), and B20 is V. Bourrier et al. (2020).

S. Vissapragada et al. 2020a). For all observations, we obtained at least five dithered frames for background correction as noted in Table 2.

We first dark-subtracted and flat-fielded all images, and then corrected for bad pixels and subtracted the sky background following S. Vissapragada et al. (2020b). Given that the bandpass of the helium filter changes across the detector field of view, different comparison stars will undergo different time-varying water absorption and OH emission (S. Vissapragada et al. 2020b, 2022). We therefore correct for telluric emission lines and the time-varying water absorption by first sigma-clipping each science frame to remove sources and then median-scaling the dithered background frame to match the science frame in 10-pixel radial steps from the zero point of the filter (where light passes through the filter at normal incidence). While this process eliminates most of the telluric background, we can use the scaling factors from this procedure to also correct for the time-varying telluric water absorption following the procedure outlined in (K. Paragas et al. 2021). In particular, we take the ratio of the scaling factors for telluric OH lines contaminated by water absorption to the telluric OH lines uncontaminated by water absorption. The ratio of these scaling factors serves as a proxy for the time-varying water absorption proxy that we can use for decorrelation in our transit lightcurve fits.

We used `photutils` (L. Bradley et al. 2023) to perform aperture photometry on both the target and nearby comparison stars that fell within WIRC’s $8 \times 8'$ field of view. As part of this step, we also subtracted any residual local sky background using annular apertures centered on the target and comparison stars with inner radii of 25 pixels ($6''25$) and outer radii of 50 pixels ($12''50$). For each observation, we determined the optimal aperture size by first normalizing the target star’s light curve using an average of the comparison star light curves and removing 4σ outliers using a moving-median filter. We then tested apertures ranging from 5 to 20 pixels in radius in 1 pixel steps (pixel scale: $0''25/\text{px}$), and selected the aperture that minimized the variance in the normalized and outlier-corrected target photometry. The optimal apertures for each target in our survey are reported in Table 2.

2.3. Light-Curve Modeling

We fit each target’s light curve with a model consisting of a transit light curve multiplied by a systematics model. We calculated the transit light curve using `exoplanet` (D. Foreman-Mackey et al. 2021, 2024), following a procedure similar to S. Vissapragada et al. (2022) and M. Saidel et al. (2025). Briefly, we modeled limb-darkened versions of our transit light curves using `starry` (R. Luger et al. 2019), where each transit light curve is parameterized by the orbital period P , the ra-

Table 2. Summary of Palomar/WIRC observations analyzed in this work.

Planet	Date (UT)	Transit Fraction	t_{exp} (s)	Start/Min/End	Airmass	n_{comp}	n_{dither}	r (px)	σ [%]	$\sigma/\sigma_{\text{phot}}$	Covariates
HAT-P-8 b	2023 Sep 21	Partial	90	1.16/1.16/2.91	3	9	12	0.75	2.3	w, a	
	2024 Aug 09	Partial	90	1.72/1.00/1.00	2	9	7	0.92	3.4	w	
WASP-93 b	2024 Jan 08	Full	90	1.13/1.13/2.41	4	5	14	0.49	1.4	p, a	
	2024 July 29	Full	90	1.54/1.05/1.06	3	5	12	0.59	1.1	-	
WASP-180 A b	2024 Dec 06	Full	90	1.98/1.22/1.70	3	5	11	0.62	2.0	a	
	2024 May 16	Full	120	2.07/1.12/1.71	3	5	10	0.85	1.0	a	
WASP-103 b	2024 May 17	Full	120	2.75/1.11/1.71	3	5	10	0.89	1.2	a	
	2025 Apr 30	Full	120	2.79/1.16/1.16	3	5	10	0.85	1.2	-	
KELT-7 b	2023 Dec 09	Full	90	1.09/1.00/1.13	3	9	13	0.17	1.9	w, a	
	2023 Dec 28	Partial	90	1.02/1.02/1.70	3	9	9	0.27	1.8	-	
WASP-12 b	2025 Feb 20	Full	90	1.08/1.00/2.92	3	9	7	0.56	1.2	a	

NOTE—In the column headers, “Transit fraction” refers to the observation of either a full or partial transit, t_{exp} is the exposure time, n_{comp} is the number of comparison stars used in the reduction, n_{dither} is the number of dithered frames used to construct the sky background frame, r is the aperture radius used in the photometric extraction, σ is the rms scatter of the residuals to our final light-curve fit, and $\sigma/\sigma_{\text{phot}}$ is the ratio of the rms scatter to the photon noise limit. The “Covariates” column displays the optimal detrending vectors in the final versions of our fits, in which “w” refers to the time-varying telluric water proxy, “a” represents airmass, “p” is psf width, and “-” refers to no covariates.

Table 3. Priors for the transit light-curve fits.

Planet	P (days)	T_0 (BJD)	b	a/R_{\star}	References
HAT-P-8 b	$\mathcal{N}(3.07634347, 0.00000058)$	$\mathcal{N}(2456052.75596, 0.00024)$	$\mathcal{N}(0.32, 0.19)$	$\mathcal{N}(6.29, 0.06)$	L09, K23
WASP-93 b	$\mathcal{N}(2.7325321, 0.0000020)$	$\mathcal{N}(2456079.56501, 0.00026)$	$\mathcal{N}(0.9036, 0.0090)$	$\mathcal{N}(5.938, 0.133)$	H16, Y24
WASP-180 A b	$\mathcal{N}(3.409264, 0.000001)$	$\mathcal{N}(2458206.519399, 0.000049)$	$\mathcal{N}(0.29, 0.02)$	$\mathcal{N}(8.75, 1.13)$	T19, K23
WASP-103 b	$\mathcal{N}(0.925545386, 0.000000056)$	$\mathcal{N}(2457308.324538, 0.000030)$	$\mathcal{N}(0.19, 0.13)$	$\mathcal{N}(3.013, 0.027)$	G14, K23
KELT-7 b	$\mathcal{N}(2.734770, 0.000004)$	$\mathcal{N}(2458827.45748, 0.00009)$	$\mathcal{N}(0.593, 0.0550)$	$\mathcal{N}(5.50, 0.17)$	S17, PE22
WASP-12 b	$\mathcal{N}(1.091418901, 0.000000018)$	$\mathcal{N}(2457607.519305, 0.000032)$	$\mathcal{N}(0.424, 0.013)$	$\mathcal{N}(3.04, 0.03)$	L24, K23

NOTE—In the references column, L09 refers to D. W. Latham et al. (2009), K23 is A. Kokori et al. (2023), H16 is K. L. Hay et al. (2016), Y24 is S. Yalçınkaya et al. (2024), T19 is L. Y. Temple et al. (2019), G14 is M. Gillon et al. (2014), S17 is K. G. Stassun et al. (2017), PE22 is J. A. Patel & N. Espinoza (2022), and L24 is P. Leonardi et al. (2024).

ratio of the planetary to stellar radius R_p/R_{\star} , the epoch T_0 , the impact parameter b , the ratio of the semi-major axis to stellar radius a/R_{\star} , the quadratic limb darkening coefficients u_1 , u_2 , and a jitter term $\log(\sigma_{\text{extra}})$ which we add in quadrature to the photon noise for each data point. We placed Gaussian priors on P , T_0 , b , and a/R_{\star} using published values from the literature as detailed in Table 3, and utilized uniform priors for R_p/R_{\star} (prior range: 0–0.25), u_1 , u_2 (sampled using the approach detailed in D. M. Kipping 2013), and $\log(\sigma_{\text{extra}})$ (prior range: 10^{-6} – 10^{-2}).

We accounted for time-varying telluric and instrumental effects by fitting a linear trend in time along with a linear combination of comparison star light curves, where the weight of each comparison star light curve is a free parameter in the fit (e.g., M. Saidel et al. 2025). We also considered four additional covariates for each observation, including the airmass, the distance from the median centroid, the psf width, and the time-varying telluric water absorption proxy. We fit each

transit light curve using all possible combinations of these four covariates and selected the version of the fit that minimized the Bayesian Information Criterion (BIC; G. Schwarz 1978). The final sets of covariates selected for each individual observation are listed in Table 2.

After selecting the optimal detrending vectors, we jointly fit the individual nights of data for each planet assuming common values for R_p/R_{\star} , u_1 , and u_2 while allowing for night-specific systematics models and noise terms. We then repeated these joint fits with fixed limb darkening coefficients calculated using `1dtk` (H. Parviainen & S. Aigrain 2015) and checked to see if our posteriors for R_p/R_{\star} were consistent with the values from the free limb darkening fits. We also checked to see if the joint probability distribution for u_1 and u_2 was consistent with the predicted values from `1dtk`. For fits that were 1σ consistent in both of these parameters (HAT-P-8 b, WASP-93 b, WASP-103 b, WASP-12 b), we adopted the fixed limb darkening coefficients in the final version

of fits, as these values are in good agreement with our empirically measured limb-darkening coefficients. For cases where the two fits were inconsistent (WASP-180 A b, KELT-7 b), we adopted the fits with limb-darkening as a free parameter. Our results are generally in good agreement with those of S. Vissapragada et al. (2022), who found that their retrieved limb-darkening coefficients were in good agreement with model predictions for most stars in their survey of He* absorption from gas giants transiting K dwarfs.

We used the Hamiltonian MCMC No U-Turn Sampler (NUTS; M. D. Hoffman & A. Gelman 2011) in `pymc3` (J. Salvatier et al. 2016) to sample the posterior probability distributions. All fits were run using four chains with 1,500 tuning steps and 2,500 draws per chain. For all fits, we confirmed that the Gelman-Rubin parameter $\hat{R} < 1.01$ for all sampled parameters, indicating the fit has converged (A. Gelman & D. B. Rubin 1992). We list the priors and posteriors for the transit light curve model fits in Table 3 and 4 respectively, and discuss results for each individual planet in more detail below. In Table 4 we also report values for the He* excess absorption at mid-transit, calculated following the methodology outlined in S. Vissapragada et al. (2022). The normalized and binned light curves for all planets are shown in Fig. 2.

3. INDIVIDUAL PLANET RESULTS

3.1. HAT-P-8 b

HAT-P-8 b (D. W. Latham et al. 2009) is an inflated hot Jupiter ($1.35 M_J$, $1.50 R_J$) with a relatively low Roche filling factor (0.23) on a 3.08 day orbit around a late F star (6200 ± 80 K, $v \sin i_* = 11.50 \pm 0.50$ km s $^{-1}$; A. S. Bonomo et al. 2017) near the Kraft break (R. P. Kraft 1967). This star is the central component of a hierarchical triple system, with a pair of stellar companions with effective temperatures of ~ 3100 K and ~ 3200 K located at a projected separation of $1.0''$ (E. B. Bechter et al. 2014; H. Ngo et al. 2015). The two companions have ΔJ of 6.59 ± 0.12 and 7.16 ± 0.15 , respectively, and therefore contribute negligible flux in our unresolved WIRC He* photometry.

We observed He* transits of HAT-P-8 b on UT August 9 2023, UT September 21 2023, and UT August 9 2024. The night of UT August 9 2023 suffered from poor weather conditions that prevented us from detecting the transit, and we therefore excluded this night from our subsequent analysis. On UT September 21 2023 we were able to observe the second half of the transit. On UT August 9 2024 night we successfully observed the first half of the transit, but deteriorating weather conditions resulted in a telescope closure that prevented us from ob-

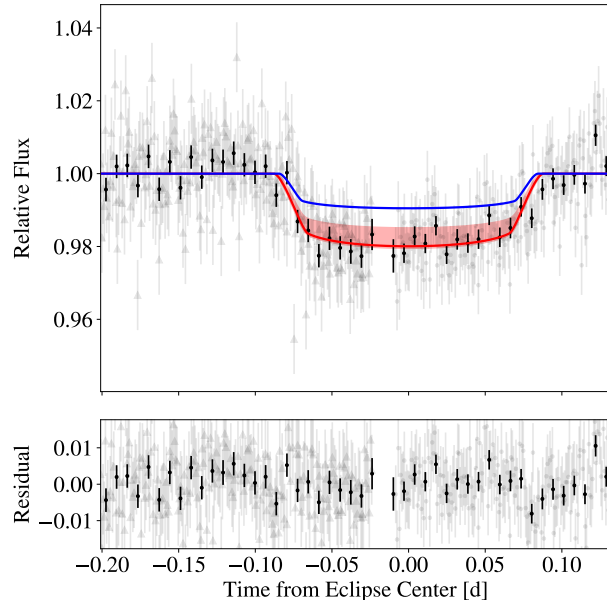
serving the second half. For this night we excluded the last fourteen science frames from our analysis, as these were taken during the poor weather conditions immediately before the telescope closure and had relatively low fluxes.

We found that the optimal covariates for the night of UT September 21 2023 are the time-varying telluric water absorption proxy and airmass, while the water absorption proxy alone is preferred on the UT August 9 2024 night. When fitting each night separately we found discrepant radius ratios of $0.035^{+0.028}_{-0.023}$ and $0.161^{+0.011}_{-0.011}$. The partial transit obtained on the first night had a shorter out-of-transit baseline and higher noise and as a result suffered from significant degeneracies that resulted in widely varying transit depths. We jointly fit both partial transits to achieve full transit coverage and minimize these degeneracies. We jointly fit both nights of data and upon comparing the retrieved transit depth to the nominal depth reported in A. Kokori et al. (2023), we find a mid-transit excess depth of $0.82^{+0.30}_{-0.30}\%$. For this fit we adopted fixed limb darkening coefficients in the final version of our fits, as the retrieved limb darkening coefficients agree with the model limb darkening coefficients within 1σ . The results of our joint fit are shown in Figure 2. Our mid-transit excess absorption corresponds to a marginally significant 2.7σ detection of an outflow, and we conclude that additional transit observations are needed to confirm this detection.

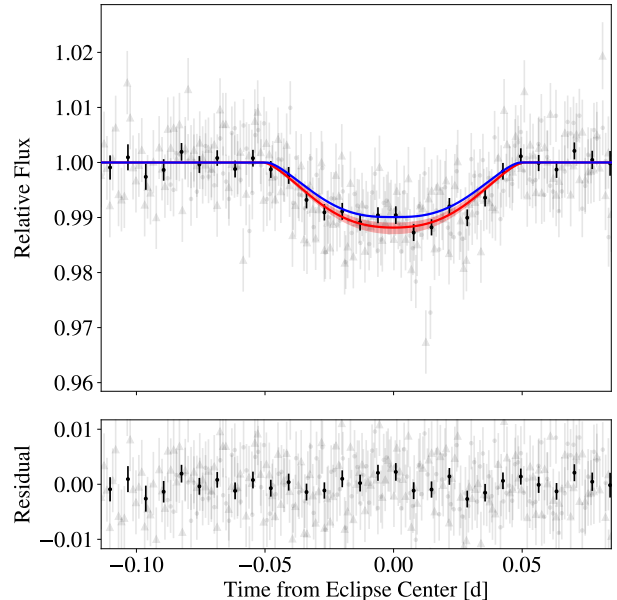
3.2. WASP-93 b

WASP-93 b is a close-in ($P = 2.73$ days) $1.47 M_J$, $1.60 R_J$ hot Jupiter orbiting a mid-F star (6700 ± 100 K; K. L. Hay et al. 2016). This planet has a relatively modest Roche filling factor (0.27), but its star has a high $v \sin i_*$ (37 ± 3 km s $^{-1}$; K. L. Hay et al. 2016) comparable to that of HAT-P-32 and HAT-P-67. K. L. Hay et al. (2016) report a nearby companion with a projected separation of $0.69''$ and $\Delta J = 3.70 \pm 0.18$. This would correspond to an early-to-mid K dwarf star if the companion is bound. The companion is unresolved in our WIRC imaging, but contributes a negligible amount of flux in the He* band.

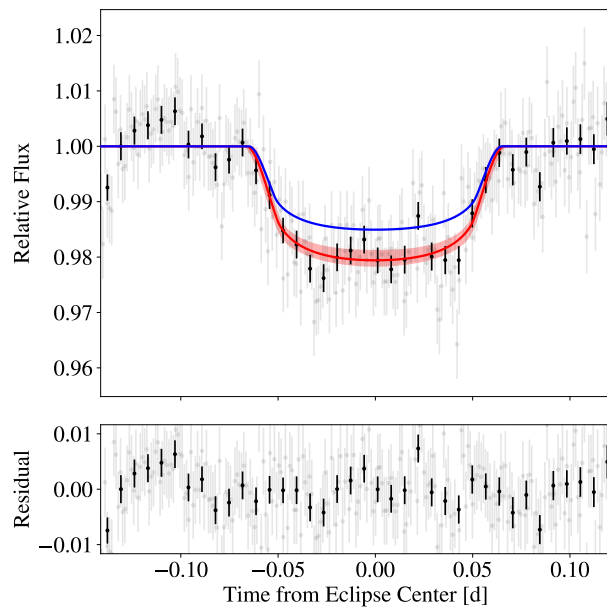
We observed transits of WASP-93 b on UT January 8 2024 and UT July 29 2024. For the night of UT January 8 2024, we found that the BIC was minimized when we fit using the airmass and psf width as additional covariates. For the night of UT July 29 2024, we did not prefer any additional covariates. We adopted fixed limb darkening coefficients in our final version of our fits, as we found that the calculated limb darkening coefficients agreed well with the joint distribution of retrieved quadratic limb darkening coefficients, and



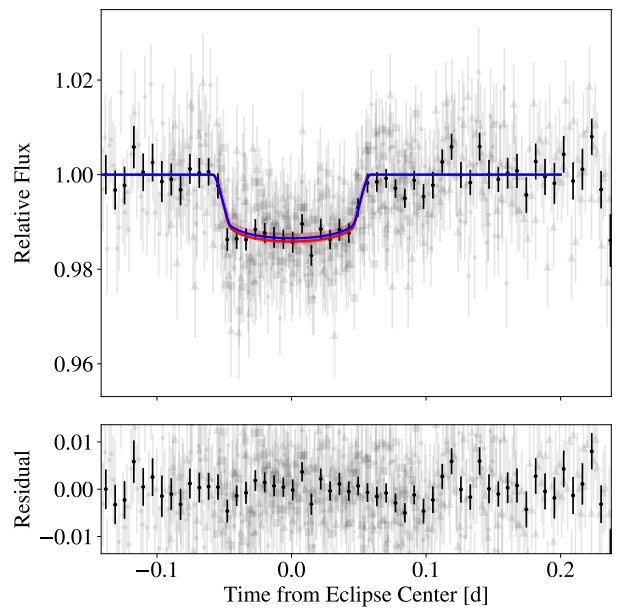
(a) HAT-P-8 b



(b) WASP-93 b



(c) WASP-180 A b



(d) WASP-103 b

our choice did not make a substantial difference for the retrieved transit depth. When fitting each night individually we retrieved radius ratios of $0.1078^{+0.0076}_{-0.0074}$ and $0.1192^{+0.0081}_{-0.0078}$, which corresponded to mid-transit excess depths of $0.052^{+0.124\%}_{-0.125\%}$ and $0.25^{+0.13\%}_{-0.13\%}$ respectively when compared to the updated transit depth reported in (A. Kokori et al. 2023). We note that while these two depths are consistent at the 1σ level, there does appear to be correlated noise at approximately mid-transit on both nights that is likely contributing to the variations in the retrieved depths. In our final joint fit, we find

a final radius ratio of $0.1172^{+0.0068}_{-0.0065}$ corresponding to a mid-transit excess depth of $0.22^{+0.11\%}_{-0.11\%}$. This is a tentative (2.0σ) outflow detection. We emphasize that this detection is tentative and requires follow-up for confirmation given that the correlated noise present in both of our observations could bias our retrieved transit depths.

3.3. WASP-180 A b

WASP-180 A b is an inflated hot Jupiter ($0.9 M_J$, $1.24 R_J$) in a retrograde orbit ($P = 3.41$ days) that transits the primary star of a visual binary with a projected sep-

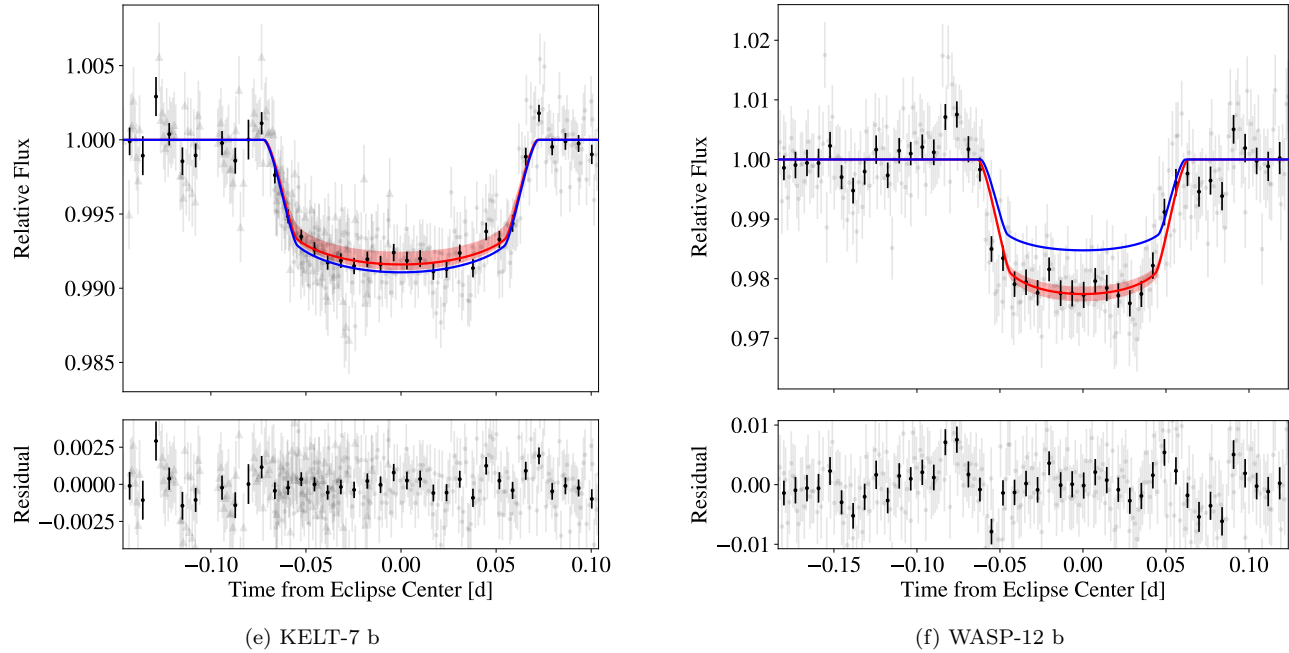


Figure 2. Transit light curves (top) and residuals (bottom) for the six planets in our survey. The detrended data (grey points, different nights have different symbol shapes) are binned to 10 minute cadence and overplotted as black circles. Our best-fit transit models are overplotted as red lines, with red shading indicating the corresponding 1σ uncertainty. The blue curves show the predicted light curve models for the case where there is no outflow.

Table 4. Posteriors for the light-curve fits.

Planet	LDC	P (days)	T_0 (BJD – 2450000)	b	a/R_\star	WIRC	R_p/R_\star	u_1	u_2	δ_{mid} (%)
HAT-P-8 b	fixed	$3.07634378^{+0.00000055}_{-0.00000055}$	$6052.75600^{+0.00024}_{-0.00024}$	$0.15^{+0.11}_{-0.13}$	$6.271^{+0.058}_{-0.058}$	$0.126^{+0.010}_{-0.011}$	0.28	0.13	$0.82^{+0.30}_{-0.30}$	
WASP-93 b	fixed	$2.73253553^{+0.00000097}_{-0.00000099}$	$6079.56504^{+0.00026}_{-0.00025}$	$0.8975^{+0.0093}_{-0.0090}$	$5.87^{+0.12}_{-0.12}$	$0.1172^{+0.0068}_{-0.0065}$	0.27	0.12	$0.22^{+0.11}_{-0.11}$	
WASP-180 A b	free	$3.40926356^{+0.00000087}_{-0.00000089}$	$8206.519398^{+0.000048}_{-0.000049}$	$0.29^{+0.02}_{-0.02}$	$9.07^{+0.38}_{-0.36}$	$0.1306^{+0.0050}_{-0.0051}$	$0.28^{+0.32}_{-0.20}$	$0.37^{+0.33}_{-0.37}$	$0.56^{+0.15}_{-0.15}$	
WASP-103 b	fixed	$0.92554513^{+0.00000036}_{-0.00000037}$	$7308.324538^{+0.000031}_{-0.000030}$	$0.137^{+0.096}_{-0.108}$	$2.905^{+0.063}_{-0.062}$	$0.1092^{+0.0046}_{-0.0047}$	0.29	0.12	$-0.0024^{+0.1151}_{-0.1129}$	
KELT-7 b	free	$2.7347652^{+0.0000016}_{-0.0000015}$	$8827.457473^{+0.000087}_{-0.000087}$	$0.587^{+0.034}_{-0.036}$	$5.56^{+0.14}_{-0.14}$	$0.0865^{+0.0032}_{-0.0033}$	$0.33^{+0.28}_{-0.23}$	$0.19^{+0.35}_{-0.35}$	$-0.086^{+0.061}_{-0.063}$	
WASP-12 b	fixed	$1.091418897^{+0.00000018}_{-0.00000018}$	$7607.519301^{+0.000031}_{-0.000033}$	$0.420^{+0.012}_{-0.013}$	$3.017^{+0.028}_{-0.028}$	$0.1434^{+0.0039}_{-0.0041}$	0.29	0.12	$0.73^{+0.12}_{-0.13}$	

NOTE—The “LDC” column denotes the choice of either free or fixed limb darkening coefficients. The mid-transit excess depth δ_{mid} is a derived parameter.

aration of $5''$ (L. Y. Temple et al. 2019). WASP-180 A has a $T_{\text{eff}} = 6500 \pm 150$ K, placing it comfortably above the Kraft break. When combined with the presence of a binary companion, WASP-180 A b’s significantly misaligned orbit suggests that this planet may be a compelling candidate for high-eccentricity migration (e.g., C. Petrovich 2015; K. R. Anderson et al. 2016; N. I. Storch et al. 2017). This star has a moderately rapid $v \sin i_\star$ (19.9 ± 0.6 km s $^{-1}$; L. Y. Temple et al. 2019) and the lowest Roche filling factor (0.20) of our survey targets.

We observed one transit observation of this planet on UT 2024 December 6. For this night, we found that the optimal covariate was the airmass. We confirmed that

the binary companion should lie outside of our nominal 11 pixel (2.7'') aperture radius, even after accounting for the diffuser-controlled PSF radius of 1.5''. We additionally found that the fixed limb darkening coefficients disagreed with the retrieved coefficients by more than 2σ , and we therefore used free limb darkening coefficients in the final version of our fits. As discussed in C. Gascón et al. (2025), the presence of extended tails in the outflow can modify the transit shape in a way that alters the preferred limb-darkening coefficients when fitting a standard transit shape to the light curve. We discuss this possibility in more detail in §5.4. Our optimized fits result in a radius ratio of $0.1306^{+0.0050}_{-0.0051}$. We compare our retrieved transit depth to the updated depth

reported in (A. Kokori et al. 2023) and find a mid-transit excess absorption of $0.56^{+0.15\%}_{-0.15\%}$. We therefore conclude that there is statistically significant (3.7σ) evidence for a He* outflow.

3.4. WASP-103 b

WASP-103 b is an ultra-short-period ($P = 22.2$ hr) hot Jupiter ($1.22 M_J$, $1.44 R_J$) orbiting an F8 star (6110 ± 160 K, $v \sin i_* = 10.6 \pm 0.9$ km s $^{-1}$; M. Gillon et al. 2014). This star has a candidate companion with a projected separation of $0''.2$ and a $\Delta J = 2.43 \pm 0.03$ (H. Ngo et al. 2016). Although this companion is not resolved in our WIRC photometry, it contributes a negligible flux in the He* bandpass. Observations of the tidally-deformed transit light curve led to a 3σ constraint on the planet's Love number ($h_f = 1.59^{+0.45}_{-0.53}$; S. C. C. Barros et al. 2022), which is similar to that of Jupiter (1.565 ± 0.006 ; D. Durante et al. 2020). WASP-103 b's inflated radius, high Roche filling factor (0.51), and high equilibrium temperature (2508 K; M. Gillon et al. 2014) make it an excellent target for atmospheric escape studies.

We observed He* transits of WASP-103 b on UT May 16 2024, UT May 17 2024, and UT April 30 2025. We obtained optimal results when we included airmass as a detrending vector for the nights of UT May 16 2024 and UT May 17 2024, and no covariates for the night of UT April 30 2025. Our optimized individual fits result in radius ratios of $0.1184^{+0.0064}_{-0.0069}$, $0.1113^{+0.0030}_{-0.0015}$, $0.100^{+0.013}_{-0.015}$ for the first, second and third nights. We note that while the first and second night radius ratios are within approximately 1σ , the third night radius ratio is discrepant and is likely a result of the significantly shorter baseline and higher noise on this night. These radius ratios translate to mid-transit excess absorption values of $0.23^{+0.18\%}_{-0.18\%}$, $0.051^{+0.076\%}_{-0.038\%}$ and $-0.22^{+0.31\%}_{-0.31\%}$ respectively. For our final fits, we adopted fixed limb darkening coefficients as the calculated limb darkening coefficients were within 1σ of the retrieved limb darkening coefficients. Jointly fitting our observations resulted in a final transit depth of $0.1092^{+0.0046}_{-0.0047}$, which we compare to the nominal transit depth reported in M. Gillon et al. (2014) to obtain a mid-transit excess absorption of $-0.0024^{+0.1151\%}_{-0.1129\%}$, corresponding to a non-detection of an outflow with a 95th-percentile upper limit of 0.19% on the excess absorption.

3.5. KELT-7 b

KELT-7 b is a $1.39 M_J$, $1.60 R_J$ hot Jupiter with a low Roche filling factor (0.26) on a close-in orbit ($P = 2.73$ days) around an early F star ($T_{\text{eff}} = 6789 \pm 50$ K; A. J. Cannon & E. C. Pickering 1918; A. Bieryla et al. 2015). Recent $3 - 5 \mu\text{m}$ transmission spectroscopy with JWST

NIRSpec indicates that this planet has an atmospheric metallicity of $1 - 16 \times$ solar, although the limited wavelength coverage of these data means that this result is partially degenerate with the assumed cloud properties (E.-M. Ahrer et al. 2025). We observed He* transits of KELT-7 b on UT December 9 2023, UT December 17 2023, and UT December 28 2023. We attempted to observe this target on one additional night (UT November 17 2023) but weather conditions were poor and we were unable to obtain useful data. Our UT December 17 2023 night was also affected by weather, which forced a closure near mid-transit with poor data quality that persisted throughout the night. We found that the transit was unrecoverable on this night, and therefore excluded it from our analysis. Our two remaining observations included a full transit on UT December 9 2023 and a partial transit on UT December 28 2023. The latter was affected by intermittent clouds during the early part of the observation, which we accounted for by excluding science frames where the flux of KELT-7 decreased below 0.6 of the median value.

We found that the optimal detrending vectors for the night of UT December 9 2023 were the time-varying telluric water proxy and airmass, while we preferred no covariates for the night of UT December 28 2023. Our optimized fits resulted in radius ratios of $0.0854^{+0.0046}_{-0.0044}$ and $0.1113^{+0.0061}_{-0.0056}$ for the first and second nights, respectively. Comparing these radius ratios to the nominal ratio reported in the discovery paper ($0.09097^{+0.00065}_{-0.00064}$; A. Bieryla et al. 2015), we found mid-transit excess absorption values of $-0.077^{+0.079\%}_{-0.080\%}$ and $0.53^{+0.14\%}_{-0.14\%}$ for the first and second night of data, respectively. We found that our calculated limb-darkening coefficient were discrepant ($> 2\sigma$) with the joint distribution of retrieved quadratic limb darkening coefficients, and we therefore adopted the free limb darkening coefficients in the final version of our fit. This star has the highest $v \sin i_*$ of all of the stars in our sample (69.3 ± 0.2 km s $^{-1}$; G. Zhou et al. 2016), and it is possible that this fast rotation causes its limb-darkening profile to deviate from the values predicted by 1D stellar models. The joint fit resulted in a radius ratio of $0.0865^{+0.0033}_{-0.0032}$, which is approximately 1σ consistent with the nominal transit depth, and corresponds to a mid-transit excess absorption of $-0.086^{+0.063\%}_{-0.061\%}$. We conclude that there is no evidence for a He* outflow from this planet, with a 95th-percentile upper limit of 0.018% on the excess absorption.

3.6. WASP-12 b

WASP-12 b is a hot Jupiter ($1.47 M_J$, $1.97 R_J$) orbiting a slowly rotating late F star (6265 ± 50 K, $v \sin i_* = 1.6^{+0.8}_{-0.4}$ km s $^{-1}$) host every 1.09 days (L. Hebb et al.

2009; S. Albrecht et al. 2012; P. Leonardi et al. 2024). WASP-12 b is the only exoplanet that has been observationally confirmed to be undergoing tidally-induced orbital decay (G. Maciejewski et al. 2016; K. C. Patra et al. 2017; N. N. Weinberg et al. 2017; A. Bailey & J. Goodman 2019; S. W. Yee et al. 2020; L. Ma & J. Fuller 2021). Measurements of the tidal deformation of WASP-12 b have resulted in an estimated Love number ($h_2 = 1.55^{+0.45}_{-0.49}$) similar to those of Jupiter and WASP-103 b (see Section 3.4), suggesting that these planets may have similar internal structures (B. Akinsanmi et al. 2024). This star is the primary in a hierarchical triple system, with a pair of early M dwarf companions located at a projected separation of $1''.06$ with ΔJ of 3.81 ± 0.05 and 3.92 ± 0.05 , respectively (E. B. Bechter et al. 2014; H. Ngo et al. 2015). These companions are not resolved in our WIRC photometry, but contribute a negligible flux in the He* aperture.

WASP-12 b's high Roche filling factor (0.55) and extreme stellar irradiation make it particularly susceptible to atmospheric loss. NUV observations reveal a deep transit signal consistent with Roche lobe overflow, with significant pre-ingress absorption indicative of extended escaping material that likely forms a torus around the star (L. Fossati et al. 2010; D. Lai et al. 2010; C. A. Haswell et al. 2012; L. Fossati et al. 2013; J. D. Nichols et al. 2015). A separate detection of H α absorption by A. G. Jensen et al. (2018) is more difficult to interpret, as subsequent H α observations with other spectrographs were unable to recover the reported signal (A. Pai Asnodkar et al. 2024; S. Czesla et al. 2024a). It has also been suggested that emission from escaping CO gas flowing from the planet onto the star might explain the shape of WASP-12 b's Spitzer 4.5 μm phase curve, which has a modulation period that is half of the planet's orbital period (T. J. Bell et al. 2019).

Two previous He* transit observations of WASP-12 b found no traces of escaping helium (L. Kreidberg & A. Oklopčić 2018; S. Czesla et al. 2024a). However, the L. Kreidberg & A. Oklopčić (2018) study used low resolution HST/WFC3 data, while the high resolution data obtained by S. Czesla et al. (2024a) is at the sensitivity limit for CARMENES. We searched for photometric evidence of escaping helium using one transit observations of WASP-12 b obtained on UT February 20 2025. We found that our systematics model for this observation was optimized when we include the airmass as a detrending vector. We adopted fixed limb darkening coefficients in the final version of the fit, as the calculated limb darkening coefficients agreed well with the retrieved limb darkening coefficients. The radius ratio obtained in our optimized transit fit is $0.1434^{+0.0039}_{-0.0041}$. Compar-

ing this value with the nominal radius ratio reported in A. Kokori et al. (2023), we find a mid-transit excess absorption of $0.73^{+0.12}_{-0.13}\%$ (5.6σ detection significance).

4. MASS LOSS MODELING

4.1. 1D Parker Wind Mass Loss Models

For our survey targets, we convert our measured He* excess absorptions into constraints on their atmospheric mass-loss rates using the `sunbather` package. This package models the atmospheric outflows as one-dimensional isothermal Parker winds (D. C. Linssen et al. 2022; D. Linssen et al. 2024). For all models, we assume the outflow is 90% hydrogen and 10% helium by number. Although outflows can be fractionated, this is much less likely to occur for planets with relatively high temperatures and correspondingly fast mass loss rates (M. Schulik & J. E. Owen 2025), and this is therefore a reasonable assumption to make for the planets in our sample.

In order to accurately model the outflows for our survey targets we must choose representative models for the stellar XUV and EUV spectra (X-ray: 5–100 \AA , EUV: 100–912 \AA), which drive the outflow by heating the uppermost layers of the atmosphere. Three of our survey targets have published measurements of their X-ray fluxes. For WASP-180 A, G. Foster & K. Poppenhaeger (2022) used an *eROSITA* observation to reconstruct the star's EUV flux and calculated a corresponding XUV flux at the planet's surface of $5.7 \times 10^5 \text{ erg s}^{-1} \text{ cm}^{-2}$. We convert this into an XUV luminosity at the stellar surface of $3.2 \times 10^{31} \text{ erg s}^{-1}$. This star has a companion with $T_{\text{eff}} = 5430 \pm 30 \text{ K}$ and a projected separation of $5''$ (L. Y. Temple et al. 2019) that is unresolved in the *eROSITA* observation. Following the methodology in Appendix A of G. Foster & K. Poppenhaeger (2022), we therefore multiplied the reported XUV flux by a factor of 0.5 to correct for the blended light from the second star. WASP-12 and KELT-7 have both been observed by *XMM-Newton*, which measured an XUV luminosity of $(4.1 \pm 0.1) \times 10^{28} \text{ erg s}^{-1}$ for KELT-7 (H. M. Tabernero et al. 2022) and an upper limit of $6 \times 10^{28} \text{ erg s}^{-1}$ for the XUV luminosity of WASP-12 (S. Czesla et al. 2024a). The remaining three survey targets (HAT-P-8, WASP-93, WASP-103) have no reported XUV observations in the literature.

We model the high-energy stellar spectra for our survey targets by adopting proxy stellar spectra from the MUSCLES survey (A. Youngblood et al. 2017) that are close matches in effective temperature and $v \sin i_*$ to the stellar hosts of our survey targets, although we note that the measured XUV luminosities of early-type stars with transiting hot Jupiters can vary by several orders

of magnitude even for stars with similar effective temperatures and $v \sin i_*$ values (see Fig. 3). For all survey targets other than WASP-103 and HAT-P-8, we adopt the MUSCLES spectrum of WASP-17 ($T_{\text{eff}} = 6550 \pm 100$ K, $v \sin i_* = 10.1^{+0.9}_{-0.8}$ km s $^{-1}$; K. G. Stassun et al. 2017; A. S. Bonomo et al. 2017) as the closest proxy. For WASP-103 and HAT-P-8, which have somewhat lower effective temperatures, we use the MUSCLES spectrum of HD 149026 ($T_{\text{eff}} = 6179 \pm 15$ K, $v \sin i_* = 6.0 \pm 0.5$ km s $^{-1}$; K. G. Stassun et al. 2017; A. S. Bonomo et al. 2017). The temperature of WASP-12 b is intermediate between those of our two proxy stars (HD 149026 and WASP-17), so we select WASP-17 as our proxy because it is a closer match in XUV luminosity to the upper limit reported for WASP-12 (see Fig. 3). For survey targets with published XUV luminosity constraints, we scale the XUV flux of the proxy spectra up or down to match the published XUV luminosity measurements. We note that the measured XUV luminosity of KELT-7 is already very close to the XUV luminosity of the proxy WASP-17, so no rescaling is needed. For WASP-12, which has a published upper bound on its XUV luminosity, we confirm that our chosen proxy (WASP-17) has a luminosity that lies below this upper bound. For WASP-180 A, we scale the XUV luminosity of WASP-17 up to match the higher value measured for this star. For the targets that do not have published XUV luminosity constraints (HAT-P-8, WASP-93, WASP-103), we carry out two separate fits. In one fit we use the nominal XUV flux of the proxy star, and in the other fit we scale the XUV fluxes of the proxy stars up to match that of HAT-P-32 in order to investigate the role of a higher XUV flux on the retrieved mass loss rate. We adopt the flux of HAT-P-32 to simulate this upper bound as it is one of the few F stars with a precisely measured XUV flux that also has a published helium outflow, we note that WASP-121 is the only other such system, but its XUV flux is slightly lower. We then use these two fits to quantify the effect of the uncertain stellar XUV luminosity on our retrieved mass loss constraints.

Following the methodology outlined in M. Saidel et al. (2025), we define a grid of mass-loss rates (\dot{M}) and thermosphere temperatures (T_0) and compute a Parker wind profile at each \dot{M} - T_0 combination. We consider uniformly sampled values of \dot{M} and T_0 between 10^9 – 10^{13} g s $^{-1}$ and 5000–11 000 K, respectively. `sunbather` uses `Cloudy` (G. J. Ferland et al. 1998, 2017) to iteratively eliminate grid models where the assumed outflow temperature and mass loss rate are inconsistent (i.e., the assumed mass loss rate requires a higher or lower outflow temperature to be physically self-consistent). For the remaining self-consistent mass loss models, `sunbather`

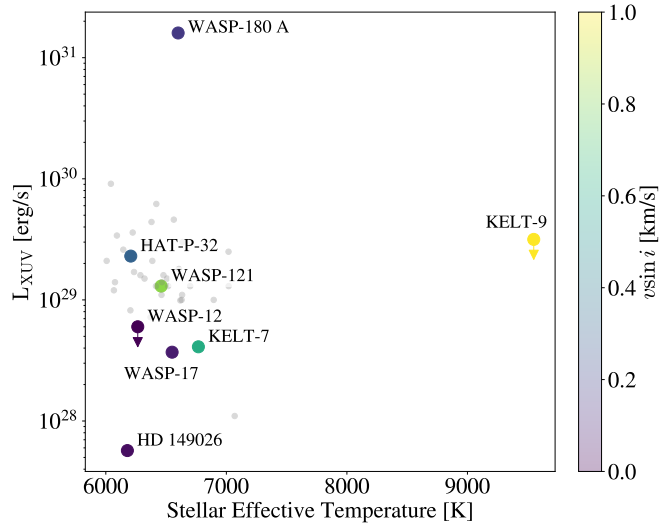


Figure 3. Published XUV luminosity as a function of stellar effective temperature for early-type stars hosting planets with detected outflows and targets in our survey (see §1 and 4.1). The XUV luminosities of the proxy MUSCLES stellar spectra used in our `sunbather` models are shown for reference. Shading corresponds to the projected stellar rotational velocities. The published XUV luminosities for WASP-12 and KELT-9 are upper bounds, which we plot here with downward pointing arrows. Gray points correspond to reported X-ray luminosities of F stars from T. Shimura et al. (2025).

uses the `Cloudy`-computed He* density profile to calculate the corresponding helium absorption signal during transit. For each model, we then integrate this signal over the 0.635 nm WIRC bandpass to calculate the predicted WIRC He* mid-transit excess absorption, which we compared to our measured values. We report the resulting best-fit mass-loss rates and thermosphere temperatures for each survey target in Table 5.

We note that the Parker wind models created using `p-winds` within `sunbather` sometimes fail to converge for a subset of grid points, likely due to known instability issues within the code base for high gravity planets (D. Linssen et al. 2025). This issue is particularly acute for WASP-103 b, where only four Parker wind models out of our entire \dot{M} - T_0 grid were successfully created and we therefore consider our retrieved mass-loss rates and temperatures to be less reliable for WASP-103. As a sanity check, we generate a `p-winds` model corresponding to the ATES-predicted mass loss rate for this planet and find an excess absorption of 0.34% in the Palomar/WIRC bandpass, which we can rule out with a 7.5σ confidence. Our `sunbather` runs for WASP-93 b also faced some convergence issues when constructing the Parker wind models, although the issue was less acute for this planet

(40 grid models were successfully created, spanning a significant fraction of the parameter space).

5. DISCUSSION

5.1. Are the Measured Mass Loss Rates Consistent with Energy-Limited Predictions?

We compare our retrieved mass-loss rates to predicted energy-limited mass-loss rates calculated using the parameterization provided in Appendix A of [A. Caldirola et al. \(2022\)](#). Following the **ATES** parameterization, we also present heating efficiencies (n_{eff}) for our predicted and retrieved mass-loss rates in Table 5. For our survey targets with unknown stellar XUV fluxes (HAT-P-8 b, WASP-93 b, WASP-103 b), we report the range of allowed mass-loss rates and thermosphere temperatures in Table 5. These ranges are calculated using our unscaled and scaled proxy stellar XUV **sunbather** model runs. In particular, the lower bounds of the allowed parameter ranges are obtained by taking the retrieved mass-loss rates and thermosphere temperatures from the unscaled models and subtracting their 1σ uncertainties. The upper bounds of the allowed temperature ranges are obtained by taking the retrieved mass-loss rates and thermosphere temperatures from the scaled XUV models and adding the 1σ uncertainties. For HAT-P-8 b and WASP-93 b, our retrieved mass-loss rate ranges agree well with the **ATES** model predictions, however our lower bounds on the retrieved mass loss rates are slightly lower than the lower bounds predicted by **ATES**. For WASP-103 b, our retrieved mass-loss rate ranges are much lower than the **ATES**-predicted mass-loss rates. We discuss possible sources of this discrepancy in Section 5.2.

For the three survey targets with published XUV flux constraints (WASP-180 A b, KELT-7 b, WASP-12 b), we find that our retrieved mass-loss rates are 1σ consistent with predictions, highlighting the importance of using a measured XUV luminosity for the host star in these mass-loss models. We carry out a similar exercise using the published mass loss rates for HAT-P-32 b and HAT-P-67 b and find that they are in good agreement with the predicted mass-loss rates when the XUV flux of the proxy star is scaled up to match the published XUV flux measurement for HAT-P-32. Similarly, for WASP-121 b, we find that the published mass-loss rate agrees well with model-predicted mass-loss rate when the proxy star is scaled to match the measured XUV flux of WASP-121. WASP-94 A b's retrieved mass-loss rate is in good agreement with our energy-limited prediction, suggesting that the unknown stellar XUV flux of the host might be similar to that of our chosen proxy, HD 149026. We therefore conclude that the measured mass-loss rates for

all of these systems appear to be broadly in agreement with our energy-limited predictions, with the caveat that the uncertainties on the stellar XUV luminosities can be quite large for stars without direct measurements.

5.2. Roche Lobe Overflow and Enhanced XUV Fluxes Drive Strong Outflows

Of the six planets in our survey, WASP-12 b is the only target that has a measured atmospheric mass-loss rate greater than 10^{12} g s^{-1} , comparable to those of HAT-P-32 b, HAT-P-67 b, WASP-33 b, WASP-121 b, and KELT-9 b ([A. Wyttenbach et al. 2020](#); [S. Czesla et al. 2022](#); [Z. Zhang et al. 2023](#); [A. Bello-Arufe et al. 2023](#); [M. Gully-Santiago et al. 2024](#); [S. Czesla et al. 2024b](#)). The remaining survey targets have much lower mass-loss rates, similar to the published constraints on the mass loss rates of WASP-48 b and WASP-94 b ([K. A. Bennett et al. 2023](#); [S. Mukherjee et al. 2025](#)) and broadly in line with the average mass-loss rates reported for gas giant planets orbiting cooler stars. We conclude that gas giants orbiting F stars do not experience systematically higher atmospheric mass-loss rates. Instead, our results suggest that mass loss rates greater than 10^{12} g s^{-1} are driven by properties that are specific to these systems. As shown in Fig. 4 and Table 1, the planets with the highest measured mass loss rates tend to have the highest Roche filling factors, indicating that RLO may play a significant role in driving these outflows.

WASP-103 b appears to be a notable exception to this trend. This planet has a Roche filling factor comparable to that of WASP-12 b, yet our retrieved upper limit on the mass loss rate for WASP-103 b is three orders of magnitude lower than the predicted value. As noted earlier, there are no published measurements of the XUV flux of this star, although its effective temperature and $vsini_*$ are very close to those of our chosen proxy star, HD 149026. This suggests that either this star has a much lower XUV flux than HD 149026, or the fraction of metastable helium in the outflow is much lower than predicted. Similarly, WASP-94 A b also has a high Roche filling factor, comparable to HAT-P-32 b, and yet it has a much lower mass loss rate, which might be a result of a much less XUV-luminous stellar host.

The importance of a high stellar XUV flux for driving outflows is supported by our detection of a He^* outflow on WASP-180 A b. Although this planet has a relatively moderate Roche filling factor of just 0.20, the host star has a higher XUV luminosity than any of the other stars in our sample with published measurements (see Fig. 3). This high XUV luminosity likely plays a significant role in generating the observed atmospheric outflow. Although KELT-7 has a similar effective tem-

Table 5. Mass loss modeling summary and results for planets with He* detections and non-detections.

Planet	Spectrum	ATES Predictions		Retrieved		
		$\log \dot{M}$ (g s $^{-1}$)	n_{eff}	$\log \dot{M}$ (g s $^{-1}$)	T_0 (K)	n_{eff}
HAT-P-8 b	HD 149026	9.96 – 10.05	0.0070 – 0.0072	9.2 – 10.9	10800 – 11000	0.0012 – 0.050
WASP-93 b	WASP-17	10.56 – 11.36	0.072 – 0.084	9.10 – 11.2	10300 – 11100	0.0016 – 0.050
WASP-180 A b	WASP-17	12.00	0.033	$11.85^{+0.2}_{-0.2}$	10600^{+300}_{-900}	2.2×10^{-4}
WASP-103 b	HD 149026	12.23 – 12.60	0.17 – 0.27	9.0 – 9.39	9700 – 11100	$(1.0 – 1.6) \times 10^{-4}$
KELT-7 b	WASP-17	10.72	0.14	$10.1^{+0.9}_{-0.5}$	10300^{+100}_{-600}	0.034
WASP-12 b	WASP-17	12.23	0.34	$12.4^{+0.6}_{-0.5}$	9800^{+600}_{-900}	0.51
Literature Measurements						
HAT-P-32 b	HD 149026	11.54 – 12.74	0.14 – 0.56	12.03, 12.56	5750, 14000	0.027 – 0.092
HAT-P-67 b	HD 149026	11.81 – 12.49	0.17 – 0.40	13.3	14000	1.5
KELT-9 b	-	-	-	12.8 ± 0.3	13200^{+800}_{-720}	-
WASP-33 b	-	-	-	$11.8^{+0.6}_{-0.5}$	12200^{+1300}_{-1000}	-
WASP-94 A b	HD 149026	10.89	0.71	$10.86^{+0.14}_{-0.19}$	5000 ± 1000	0.65
WASP-121 b	WASP-17	12.52	0.20	12.7 ± 0.1	^a	-

Note: The “spectrum” column refers to the proxy MUSCLES stellar spectrum used. For planets in which multiple `sunbather` models were executed (HAT-P-8 b, WASP-93 b, WASP-103 b) we report the predicted and retrieved quantities as ranges reflecting the unscaled and scaled XUV flux model runs. For planets with mass loss measurements from the literature, the “Retrieved” mass-loss rates and thermosphere temperatures are taken from the published studies cited in §1, some of which used different stellar models than the ones we use here to calculate their predicted mass loss rates. ^a S. Czesla et al. (2024b) determined the mass loss rate for this planet by fitting a 3D outflow model with a spatially varying temperature structure.

perature and a much higher $vsini_*$ value than WASP-180 A, its XUV luminosity is approximately 3 orders of magnitude lower. This underscores our conclusion in §4.1 that effective temperature and $vsini_*$ alone are imperfect predictors of XUV luminosity and reinforces the importance of star-specific XUV measurements for interpreting atmospheric mass loss constraints.

For all targets, we evaluate the role of NUV flux in driving the measured mass loss rates by calculating the NUV flux (1750–3000 Å) at the planets’ orbits using PHOENIX model spectra (T. O. Husser et al. 2013) and plotting the resulting values versus Roche filling factor in Fig. 5. For each star, we chose the PHOENIX grid model that was closest in effective temperature, surface gravity, and metallicity. We find that there is no clear correlation between NUV flux and the observed mass loss rates. This is nicely illustrated by WASP-180 A b, which has a low Roche filling factor and a low NUV flux, yet has a high measured mass loss rate that can only be explained by its high XUV flux. This suggests that Balmer-driven escape is unlikely to be the dominant escape mechanism for most of the planets in our sample.

5.3. Comparison to Published He* Observations of WASP-12 b

Of the six targets in our survey, only WASP-12 b has a published constraint on the He* excess absorption. As discussed in Section 3.6, both HST/WFC3 and CARMENES did not detect He* absorption (L. Kreidberg & A. Oklopčić 2018; S. Czesla et al. 2024a) despite repeated NUV detections of an escaping atmo-

sphere (L. Fossati et al. 2010; C. A. Haswell et al. 2012; J. D. Nichols et al. 2015). While the low resolution of HST/WFC3 could explain the non-detection reported by L. Kreidberg & A. Oklopčić (2018) the high resolution non-detection reported by S. Czesla et al. (2024a) is puzzling given our strong excess He* measurement. Using the best-fit model from our `sunbather` fits, we find that the predicted peak excess absorption in the spectroscopically resolved He* line is 6%. We compare this peak absorption to the transmission spectrum presented in Figure 5 of S. Czesla et al. (2024a) and find that this signal should have been readily detectable in their observations.

Given our high measured mass loss rate for this planet, it is possible that it might have extended absorption prior to ingress or after egress, which could result in some self-subtraction of the measured helium signal if the chosen reference baseline significantly overlaps with this extended absorption. The CARMENES observations presented in S. Czesla et al. (2024a) have a time range of –2.4 to +3.0 hours around the transit center, whereas our observations extend from –4.8 to +3.0 hours around the transit center (transit duration: 3.0010 ± 0.0043 hours; P. Leonardi et al. 2024). This self-subtraction can bias the inferred signal, but it is unlikely to be strong enough to reconcile the non-detection in S. Czesla et al. (2024b) with our Palomar observation.

Alternatively, the discrepancy between our strong excess He* measurement and the non-detection reported by S. Czesla et al. (2024a) might be resolved if the WASP-12 system contains a time-varying circumstellar torus of gas fed by the strong outflow from WASP-12

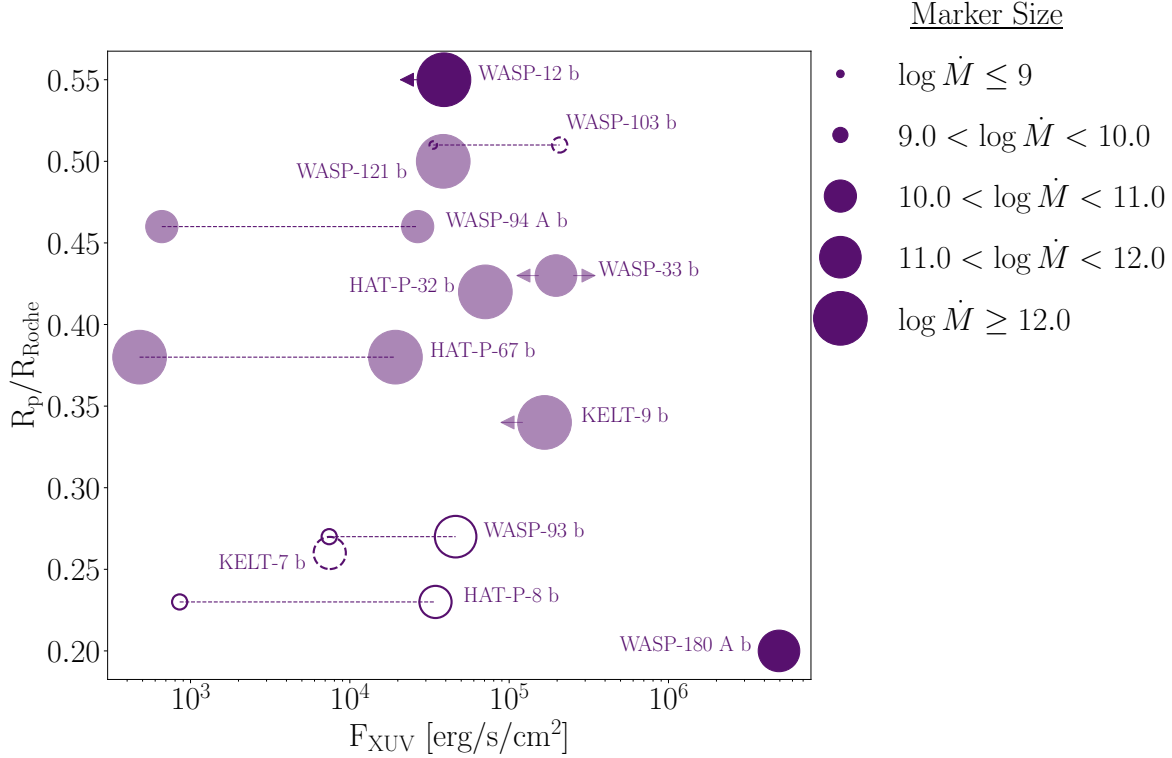


Figure 4. Roche filling factor as a function of XUV flux at the planet’s orbit for survey targets and planets orbiting early-type stars with published mass loss measurements. Filled circles correspond to robust ($\geq 3\sigma$) detections of atmospheric escape, open circles correspond to tentative ($\leq 2\sigma$) detections of atmospheric escape, open circles with dashed edges indicate non-detections. Published detections are shown as a lighter shade of purple. Point size is proportional to the retrieved mass loss rate, indicated by the legend. The published XUV luminosities for WASP-12 and KELT-9 are upper bounds and therefore the XUV fluxes at the planets’ orbits are also upper bounds, which we symbolize here with horizontal arrows. WASP-33 does not have a published XUV luminosity, so we have assigned this star the same XUV luminosity as KELT-9, the only other A-star in this sample, when calculating the XUV flux at the planet. We have indicated with arrows that the actual XUV flux may be higher or lower than this estimate. For F-type stars without published XUV luminosities (HAT-P-67, HAT-P-8, WASP-93, WASP-103, WASP-94 A), we plot two points connected by a horizontal dashed line. The lower bound corresponds to a flux calculated using the proxy star XUV luminosity (see Table 5 for proxy star choice) and the upper bound corresponds to a flux calculated using the XUV luminosity of HAT-P-32. Palomar survey targets in this set (HAT-P-8, WASP-93, WASP-103) have point sizes corresponding to the retrieved mass-loss rates calculated at each luminosity value.

b. WASP-12 b has a high inferred mass loss rate in our Palomar observation, suggesting that gas might accumulate around its host star faster than it can be dispersed by the stellar wind. If WASP-12 b’s exosphere transits across a region of the stellar disk that is already obscured by the circumstellar torus, the exospheric He^* absorption signal would be reduced, potentially rendering it undetectable (E. Schreyer & R. Murray-Clay 2025.). In order to reconcile the S. Czesla et al. (2024a) non-detections from 2019 and 2020 with the detection presented here, the column density of the circumstellar torus must vary over years-long timescales, with a higher column density during the S. Czesla et al. (2024a) observations. The time evolution of a circumstellar torus over such timescales is uncertain, and hydrodynamic models spanning these timescales are needed to fully explore this topic. However, E. Schreyer & R. Murray-

Clay (2025,) used simple arguments to calculate an approximate timescale for sufficient gas to accumulate and shield WASP-12 from the XUV radiation that drives atmospheric escape, thereby halting the supply of gas to the torus and possibly causing it to become unstable. They found that this timescale is on the order of a year, suggesting that this mechanism can potentially explain the discrepancy between these two observations.

5.4. 3D Outflow Geometry

While our photometric detections provide constraints on the mass-loss rates for our survey targets, the three-dimensional geometry of these outflows is not well constrained by our observations. As discussed in S. Vissapragada et al. (2024), extended tails of escaping atmospheric material can have low He^* optical depths, making it difficult to detect them in the photometric Palomar

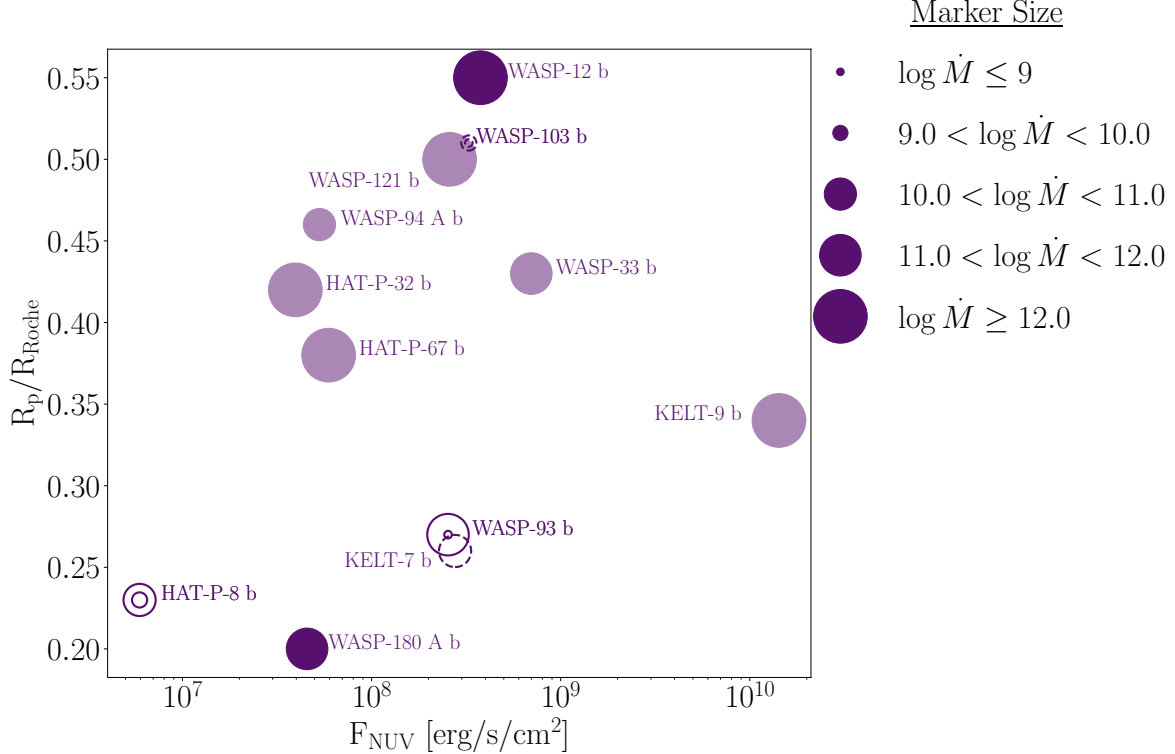


Figure 5. Roche filling factor as a function of NUV flux at the planet’s orbit for survey targets and planets orbiting early-type stars with published mass loss measurements. See the Fig. 4 caption for additional details.

mar/WIRC bandpass. Spectroscopically resolved observations of the He^* line are much more sensitive to the presence of extended absorption pre- and post-transit (e.g., J. J. Spake et al. 2021; S. Czesla et al. 2022).

In the absence of direct observational constraints, we can still make predictions for the outflow morphologies of the planets in our sample. M. MacLeod et al. (2025) showed that a planet’s predicted Rossby number (defined as a velocity v over the product of a length scale L with an orbital angular speed Ω : $v/\Omega L$) can be used to predict the morphologies of planetary outflows. This study adopts the Hill sphere (r_H) as the relevant length scale and the sound speed (c_s) as the relevant velocity:

$$R_{o,H} = \frac{c_s}{\Omega r_H}. \quad (1)$$

When $R_{o,H} \gg 1$, outflowing gas quickly expands radially away from the planet in nearly every direction, creating a large scale-height outflow that resembles a bubble (see top panel of Figure 1 in M. MacLeod et al. 2025). For $R_{o,H} \lesssim 1$, the Coriolis acceleration deviates the outflow before it can significantly expand around the planet, the outflow is then sheared into tidal tails by the differential rotation of the Keplerian orbits, resulting in a stream or tail-like outflow morphology (see bottom panel of Figure 1 in M. MacLeod et al. 2025).

We use estimated outflow sound speeds from D. Linsen et al. (2025) to compute $R_{o,H}$ for our survey targets (Figure 6) and find that all of them should have stream-like morphologies. If these planets have outflows sheared into tidal tails, there could be additional He^* absorption outside of the nominal transit window that is undetectable in our Palomar/WIRC observations. In the future, spectroscopically resolved observations with significant pre- and post-transit baseline could provide tighter constraints on the presence and extent of tail-like morphologies in these systems. Spectroscopic observations can also provide useful information on the kinematics of the outflow (from the line shifts) and the temperature of the outflow (from the line width), providing a more complete picture of the outflow dynamics.

6. CONCLUSIONS

In this work, we present the first survey of atmospheric escape on planets orbiting F stars. Using Palomar/WIRC, we obtained He^* transits of six close-in gas giants over the course of two years. We obtain two strong ($> 3\sigma$) detections of atmospheric escape for WASP-12 b and WASP-180 A b, two tentative ($2 - 3\sigma$) detections of atmospheric escape for HAT-P-8 b, and WASP-93 b, and place upper bounds on the atmospheric escape rates of WASP-103 b and KELT-7 b. We fit

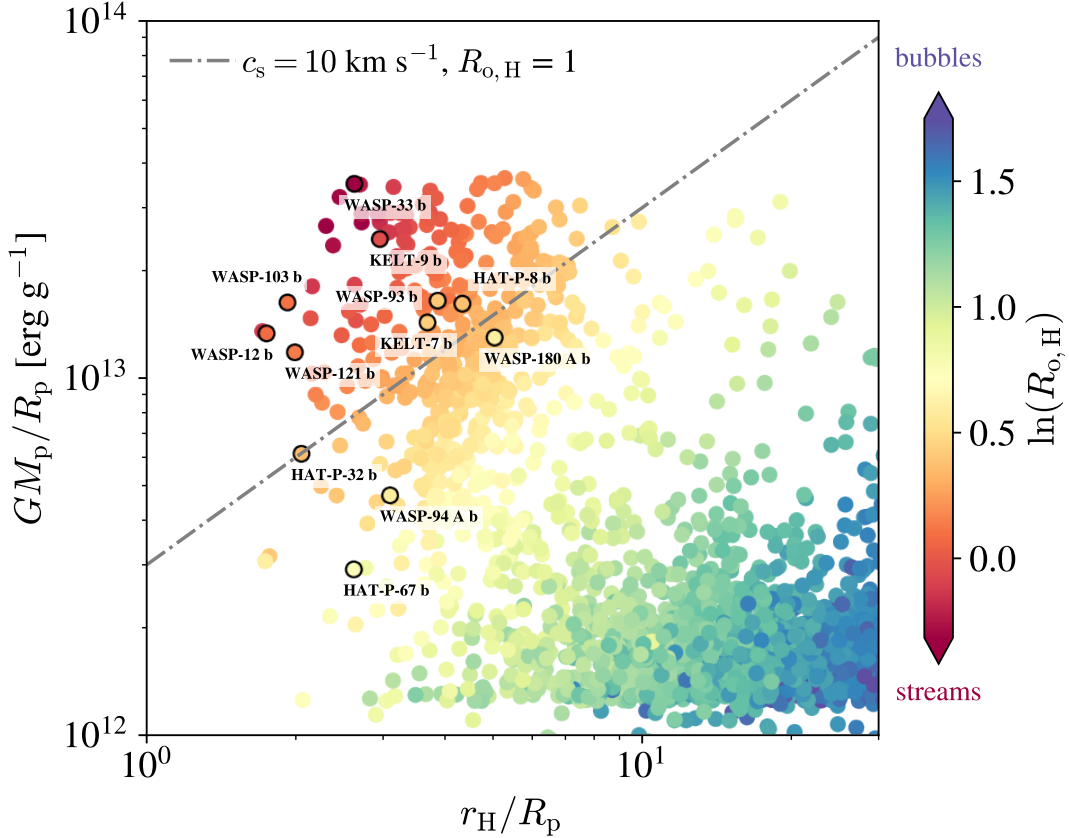


Figure 6. Figure adapted from M. MacLeod et al. (2025) and compiled using `PWMorphology`. Colored circles represent confirmed exoplanets with radii greater than $1.6R_{\oplus}$ from the `sunset` catalog shown as a function of gravitational potential and the ratio of the Hill to planet radius. Survey targets as well as HAT-P-32 b, HAT-P-67 b, KELT-9 b, WASP-33 b, WASP-94 A b, and WASP-121 b are indicated with circles outlined in black and labeled appropriately. The different colors represent the predicted hill sphere Rossby number $\ln(R_{o,H})$, where $\ln(R_{o,H}) > 0$ indicates a bubble-like outflow geometry and $\ln(R_{o,H}) < 0$ indicates a stream or tail-like outflow geometry. We note that values of $\ln(R_{o,H})$ for HAT-P-32 b, HAT-P-67 b, KELT-9 b, WASP-33 b, WASP-94 A b, and WASP-121 b are calculated using the `sunset` photoevaporative outflow models for these planets. The dashed grey line indicates photoevaporative outflows with sound speeds of 10 km s^{-1} and $R_{o,H} = 1$.

our measured He^* excess absorption values with an energetically self-consistent 1D Parker wind model using the `sunbather` package, and find that WASP-12 b and WASP-180 A b have corresponding mass loss rates of $\log \dot{M} = 12.4^{+0.6}_{-0.5} (\text{g s}^{-1})$ and $\log \dot{M} = 11.85^{+0.2}_{-0.2} (\text{g s}^{-1})$ respectively, comparable to the fast outflows reported in the literature for most other planets orbiting early-type stars. Our mass loss constraints for our other four survey targets (HAT-P-8 b, WASP-93 b, WASP-103 b, and KELT-7 b) are similar to published measurements for WASP-48 b and WASP-94 A b, which also orbit early-type stars, and are broadly in line with measured mass loss rates for gas giants orbiting cooler stars. This suggests that the strong outflows reported in the literature for planets orbiting early-type stars are not representative of all early-type systems. We do not see any evidence for a correlation between the measured mass loss rate and the NUV flux received by the planet, which

suggests that Balmer-driven escape is not the dominant driver of atmospheric escape for most planets in our sample. However, the high NUV stellar fluxes that power Balmer-driven escape also depopulate He^* . As a result, He^* observations might not be the optimal tracer to use for this particular escape process. Instead, transmission spectroscopy of Balmer absorption lines is likely more suitable for quantifying the efficacy of NUV-powered escape on a population level. Notably, the mass loss measurement for KELT-9 b, which has the highest NUV flux of all the planets in our sample, was obtained using these lines (A. Wyttenbach et al. 2020).

We combine our sample of retrieved mass loss rates with mass loss measurements from the literature to explore the factors that determine outflow strength in these systems. We find that the planets with the highest Roche filling factors tend to have the highest measured mass loss rates, although our non-detection of an outflow

for WASP-103 b is a puzzling exception to this trend. WASP-180 A b has a relatively low Roche filling factor and an anomalously high measured XUV luminosity, and our detection of an outflow on this planet demonstrates the importance of XUV luminosity as a second variable controlling outflow strength. We find that effective temperature and $vsini_*$ are not strongly correlated with XUV luminosity for the stars in our sample, underscoring the importance of direct measurements of XUV luminosities for the host stars of planets with detected outflows. Notably, WASP-103 does not have a measured XUV luminosity and our non-detection of an outflow in this system could be explained by a lower-than-expected XUV flux.

Our photometric He* observations are relatively insensitive to the presence of extended outflow structures similar to those observed for HAT-P-32 b and HAT-P-67 b (Z. Zhang et al. 2023; M. Gully-Santiago et al. 2024). Instead, we use a simple scaling law to predict the 3D outflow geometries for all of our survey targets. We find that all of them should have tail-like outflow morphologies, some of which may be detectable in spectroscopically resolved observations with extended baselines.

Our detection of a strong outflow from WASP-12 b is surprising, as this planet's spectroscopically resolved He* signal was observed in 2019 and 2020 with CARMENES, resulting in a non-detection (S. Czesla et al. 2024a). The mass loss model that provides the best fit to our Palomar/WIRC He* excess absorption has a peak excess absorption of 6%, which should have been easily detectable with CARMENES. If the outflow from this planet forms an extended torus around the star, the discrepancy between our strong detection and the CARMENES non-detection might potentially be explained by temporal variability in the disk properties. If the planet was observed during a period where the gas density in the torus was relatively high, it could obscure the He* outflow from the planet. This could be tested

by long-term monitoring of the stellar He* line equivalent width over a period of multiple years. This planet's He* absorption will be re-measured as part of upcoming JWST NIRISS/SOSS transit observations, providing another data point on this timeseries.

ACKNOWLEDGMENTS

This material is based upon work supported by the National Science Foundation Graduate Research Fellowship Program under Grant No. DGE-1745301. Any opinions, findings, and conclusions or recommendations expressed in this material are those of the author(s) and do not necessarily reflect the views of the National Science Foundation. This research made use of `nep-des` (available in <https://github.com/castro-gzlx/nep-des>). Co-author WGL gratefully acknowledges support from the Department of Defense's National Defense Science & Engineering Graduate (NDSEG) Fellowship. WGL also thanks the LSST-DA Data Science Fellowship Program, which is funded by LSST-DA, the Brinson Foundation, the WoodNext Foundation, and the Research Corporation for Science Advancement Foundation; his participation in the program has benefited this work.

We thank James Owen and Ruth Murray-Clay for their informative discussion. We also thank the Palomar Observatory telescope and support operators for their support of this work, with special thanks to Tom Barlow, Carolyn Heffner, Isaac Wilson, Diana Roderick, Paul Neid, Kathleen Koviak, Rigel Rafto, and John Stone.

Facilities: ADS, Exoplanet Archive, Hale

Software: ATES (A. Caldiroli et al. 2021), `ldtk` (H. Parviainen & S. Aigrain 2015), `nep-des` (A. Castro-González et al. 2024), `photutils` (L. Bradley et al. 2023), `p-winds` (L. A. Dos Santos et al. 2022), `PWMorphology` (M. MacLeod et al. 2025), `pymc3` (J. Salvatier et al. 2016), `sunbather` (D. Linssen et al. 2024)

REFERENCES

Addison, B. C., Tinney, C. G., Wright, D. J., & Bayliss, D. 2016, *The Astrophysical Journal*, 823, 29, doi: [10.3847/0004-637X/823/1/29](https://doi.org/10.3847/0004-637X/823/1/29)

Ahrer, E.-M., Fairman, C., Kirk, J., et al. 2025, arXiv e-prints, arXiv:2509.12479, <https://arxiv.org/abs/2509.12479>

Akeson, R. L., Chen, X., Ciardi, D., & et al. 2013, *Publications of the Astronomical Society of the Pacific*, 125, 989, doi: [10.1086/672273](https://doi.org/10.1086/672273)

Akinsanmi, B., Barros, S. C. C., Lendl, M., & et al. 2024, *Astronomy and Astrophysics*, 685, A63, doi: [10.1051/0004-6361/202348502](https://doi.org/10.1051/0004-6361/202348502)

Albrecht, S., Winn, J. N., Johnson, J. A., & et al. 2012, *The Astrophysical Journal*, 757, 18, doi: [10.1088/0004-637X/757/1/18](https://doi.org/10.1088/0004-637X/757/1/18)

Anderson, K. R., Storch, N. I., & Lai, D. 2016, *Monthly Notices of the Royal Astronomical Society*, 456, 3671, doi: [10.1093/mnras/stv2906](https://doi.org/10.1093/mnras/stv2906)

Bailey, A., & Goodman, J. 2019, Monthly Notices of the Royal Astronomical Society, 482, 1872, doi: [10.1093/mnras/sty2805](https://doi.org/10.1093/mnras/sty2805)

Barros, S. C. C., Akinsanmi, B., Boué, G., & et al. 2022, Astronomy and Astrophysics, 657, A52, doi: [10.1051/0004-6361/202142196](https://doi.org/10.1051/0004-6361/202142196)

Bechter, E. B., Crepp, J. R., Ngo, H., et al. 2014, ApJ, 788, 2, doi: [10.1088/0004-637X/788/1/2](https://doi.org/10.1088/0004-637X/788/1/2)

Bell, T. J., Zhang, M., Cubillos, P. E., & et al. 2019, Monthly Notices of the Royal Astronomical Society, 489, 1995, doi: [10.1093/mnras/stz2018](https://doi.org/10.1093/mnras/stz2018)

Bello-Arufe, A., Knutson, H. A., Mendonça, J. M., et al. 2023, AJ, 166, 69, doi: [10.3847/1538-3881/acd935](https://doi.org/10.3847/1538-3881/acd935)

Bennett, K. A., Redfield, S., Oklopčić, A., et al. 2023, AJ, 165, 264, doi: [10.3847/1538-3881/acd34b](https://doi.org/10.3847/1538-3881/acd34b)

Bieryla, A., Collins, K., Beatty, T. G., & et al. 2015, The Astronomical Journal, 150, 12, doi: [10.1088/0004-6256/150/1/12](https://doi.org/10.1088/0004-6256/150/1/12)

Bonomo, A. S., Desidera, S., Benatti, S., & et al. 2017, Astronomy and Astrophysics, 602, A107, doi: [10.1051/0004-6361/201629882](https://doi.org/10.1051/0004-6361/201629882)

Bourrier, V., Ehrenreich, D., Lendl, M., et al. 2020, A&A, 635, A205, doi: [10.1051/0004-6361/201936640](https://doi.org/10.1051/0004-6361/201936640)

Bradley, L., Sipőcz, B., Robitaille, T., & et al. 2023, 1.7.0 Zenodo, doi: [10.5281/zenodo.7804137](https://doi.org/10.5281/zenodo.7804137)

Caldirola, A., Haardt, F., Gallo, E., & et al. 2022, Astronomy and Astrophysics, 663, A122, doi: [10.1051/0004-6361/202142763](https://doi.org/10.1051/0004-6361/202142763)

Caldirola, A., Haardt, F., Gallo, E., et al. 2021, A&A, 655, A30, doi: [10.1051/0004-6361/202141497](https://doi.org/10.1051/0004-6361/202141497)

Cannon, A. J., & Pickering, E. C. 1918, Annals of Harvard College Observatory, 91, 1

Casasayas-Barris, N., Pallé, E., Yan, F., et al. 2019, A&A, 628, A9, doi: [10.1051/0004-6361/201935623](https://doi.org/10.1051/0004-6361/201935623)

Castro-González, A., Bourrier, V., & et al. 2024, Astronomy and Astrophysics, 689, A250, doi: [10.1051/0004-6361/202450957](https://doi.org/10.1051/0004-6361/202450957)

Chakrabarty, A., & Sengupta, S. 2019, The Astronomical Journal, 158, 39, doi: [10.3847/1538-3881/ab24dd](https://doi.org/10.3847/1538-3881/ab24dd)

Christiansen, J. L., McElroy, D. L., Harbut, M., & et al. 2025, arXiv e-prints, arXiv:2506.03299, doi: [10.48550/arXiv.2506.03299](https://doi.org/10.48550/arXiv.2506.03299)

Collier Cameron, A., Guenther, E., Smalley, B., et al. 2010, MNRAS, 407, 507, doi: [10.1111/j.1365-2966.2010.16922.x](https://doi.org/10.1111/j.1365-2966.2010.16922.x)

Czesla, S., Lampón, M., Cont, D., & et al. 2024a, Astronomy and Astrophysics, 683, A67, doi: [10.1051/0004-6361/202348107](https://doi.org/10.1051/0004-6361/202348107)

Czesla, S., Lampón, M., Sanz-Forcada, J., & et al. 2022, Astronomy and Astrophysics, 657, A6, doi: [10.1051/0004-6361/202039919](https://doi.org/10.1051/0004-6361/202039919)

Czesla, S., Nail, F., Lavail, A., et al. 2024b, A&A, 692, A230, doi: [10.1051/0004-6361/202451003](https://doi.org/10.1051/0004-6361/202451003)

Delrez, L., Santerne, A., Almenara, J. M., et al. 2016, MNRAS, 458, 4025, doi: [10.1093/mnras/stw522](https://doi.org/10.1093/mnras/stw522)

Dos Santos, L. A. 2023, in IAU Symposium, Vol. 370, Winds of Stars and Exoplanets, ed. A. A. Vidotto, L. Fossati, & J. S. Vink, 56–71, doi: [10.1017/S1743921322004239](https://doi.org/10.1017/S1743921322004239)

Dos Santos, L. A., Vidotto, A. A., Vissapragada, S., & et al. 2022, Astronomy and Astrophysics, 659, A62, doi: [10.1051/0004-6361/202142038](https://doi.org/10.1051/0004-6361/202142038)

Durante, D., Parisi, M., Serra, D., & et al. 2020, Geophysical Research Letters, 47, e86572, doi: [10.1029/2019GL086572](https://doi.org/10.1029/2019GL086572)

Ferland, G. J., Chatzikos, M., & et al. 2017, Revista Mexicana de Astronomía y Astrofísica, 53, 385, doi: [10.48550/arXiv.1705.10877](https://doi.org/10.48550/arXiv.1705.10877)

Ferland, G. J., Korista, K. T., & et al. 1998, Publications of the Astronomical Society of the Pacific, 110, 761, doi: [10.1086/316190](https://doi.org/10.1086/316190)

Foreman-Mackey, D., Luger, R., Agol, E., & et al. 2021, The Journal of Open Source Software, 6, 3285, doi: [10.21110/joss.03285](https://doi.org/10.21110/joss.03285)

Foreman-Mackey, D., Luger, R., Agol, E., & et al. 2024, v0.6.0 Zenodo, doi: [10.5281/zenodo.1998447](https://doi.org/10.5281/zenodo.1998447)

Fossati, L., Ayres, T. R., Haswell, C. A., & et al. 2013, The Astrophysical Journal, 766, L20, doi: [10.1088/2041-8205/766/2/L20](https://doi.org/10.1088/2041-8205/766/2/L20)

Fossati, L., Haswell, C. A., Froning, C. S., & et al. 2010, The Astrophysical Journal, 714, L222, doi: [10.1088/2041-8205/714/2/L222](https://doi.org/10.1088/2041-8205/714/2/L222)

Foster, G., & Poppenhaeger, K. 2022, Astronomische Nachrichten, 343, e20007, doi: [10.1002/asna.20220007](https://doi.org/10.1002/asna.20220007)

Fulton, B. J., Petigura, E. A., Howard, A. W., & et al. 2017, The Astronomical Journal, 154, 109, doi: [10.3847/1538-3881/aa80eb](https://doi.org/10.3847/1538-3881/aa80eb)

García Muñoz, A., & Schneider, P. C. 2019, The Astrophysical Journal, 884, L43, doi: [10.3847/2041-8213/ab498d](https://doi.org/10.3847/2041-8213/ab498d)

Gascón, C., López-Morales, M., Vissapragada, S., et al. 2025, arXiv e-prints, arXiv:2508.14846, doi: [10.48550/arXiv.2508.14846](https://doi.org/10.48550/arXiv.2508.14846)

Gaudi, B. S., Stassun, K. G., Collins, K. A., et al. 2017, Nature, 546, 514, doi: [10.1038/nature22392](https://doi.org/10.1038/nature22392)

Gelman, A., & Rubin, D. B. 1992, Statistical Science, 7, 457, doi: [10.1214/ss/1177011136](https://doi.org/10.1214/ss/1177011136)

Gillon, M., Anderson, D. R., Collier-Cameron, A., & et al. 2014, Astronomy and Astrophysics, 562, L3, doi: [10.1051/0004-6361/201323014](https://doi.org/10.1051/0004-6361/201323014)

Gully-Santiago, M., Morley, C. V., Luna, J., & et al. 2024, *The Astronomical Journal*, 167, 142, doi: [10.3847/1538-3881/ad1ee8](https://doi.org/10.3847/1538-3881/ad1ee8)

Haswell, C. A., Fossati, L., Ayres, T., & et al. 2012, *The Astrophysical Journal*, 760, 79, doi: [10.1088/0004-637X/760/1/79](https://doi.org/10.1088/0004-637X/760/1/79)

Hay, K. L., Collier-Cameron, A., Doyle, A. P., & et al. 2016, *Monthly Notices of the Royal Astronomical Society*, 463, 3276, doi: [10.1093/mnras/stw2090](https://doi.org/10.1093/mnras/stw2090)

Hebb, L., Collier-Cameron, A., Loeillet, B., & et al. 2009, *The Astrophysical Journal*, 693, 1920, doi: [10.1088/0004-637X/693/2/1920](https://doi.org/10.1088/0004-637X/693/2/1920)

Hoeijmakers, H. J., Ehrenreich, D., Kitzmann, D., et al. 2019, *A&A*, 627, A165, doi: [10.1051/0004-6361/201935089](https://doi.org/10.1051/0004-6361/201935089)

Hoffman, M. D., & Gelman, A. 2011, arXiv e-prints, arXiv:1111.4246, doi: [10.48550/arXiv.1111.4246](https://doi.org/10.48550/arXiv.1111.4246)

Husser, T. O., Wende-von Berg, S., Dreizler, S., et al. 2013, *A&A*, 553, A6, doi: [10.1051/0004-6361/201219058](https://doi.org/10.1051/0004-6361/201219058)

Jackson, B., Arras, P., Penev, K., Peacock, S., & Marchant, P. 2017, *ApJ*, 835, 145, doi: [10.3847/1538-4357/835/2/145](https://doi.org/10.3847/1538-4357/835/2/145)

Jensen, A. G., Cauley, P. W., Redfield, S., Cochran, W. D., & Endl, M. 2018, *The Astronomical Journal*, 156, 154, doi: [10.3847/1538-3881/aadca7](https://doi.org/10.3847/1538-3881/aadca7)

Jensen, A. G., Redfield, S., Endl, M., et al. 2012, *ApJ*, 751, 86, doi: [10.1088/0004-637X/751/2/86](https://doi.org/10.1088/0004-637X/751/2/86)

Kempton, E. M. R., & Knutson, H. A. 2024, *Reviews in Mineralogy and Geochemistry*, 90, 411, doi: [10.2138/rmg.2024.90.12](https://doi.org/10.2138/rmg.2024.90.12)

Kipping, D. M. 2013, *Monthly Notices of the Royal Astronomical Society*, 435, 2152, doi: [10.1093/mnras/stt1435](https://doi.org/10.1093/mnras/stt1435)

Kokori, A., Tsiaras, A., Edwards, B., & et al. 2023, *The Astrophysical Journal Supplement Series*, 265, 4, doi: [10.3847/1538-4365/ac9da4](https://doi.org/10.3847/1538-4365/ac9da4)

Koskinen, T. T., Lavvas, P., Huang, C., et al. 2022, *ApJ*, 929, 52, doi: [10.3847/1538-4357/ac4f45](https://doi.org/10.3847/1538-4357/ac4f45)

Kraft, R. P. 1967, *The Astrophysical Journal*, 150, 551, doi: [10.1086/149359](https://doi.org/10.1086/149359)

Kreidberg, L., & Oklopčić, A. 2018, *Research Notes of the American Astronomical Society*, 2, 44, doi: [10.3847/2515-5172/aac887](https://doi.org/10.3847/2515-5172/aac887)

Lai, D., Helling, C., & van den Heuvel, E. P. J. 2010, *The Astrophysical Journal*, 721, 923, doi: [10.1088/0004-637X/721/2/923](https://doi.org/10.1088/0004-637X/721/2/923)

Latham, D. W., Bakos, G. Á., Torres, G., & et al. 2009, *The Astrophysical Journal*, 704, 1107, doi: [10.1088/0004-637X/704/2/1107](https://doi.org/10.1088/0004-637X/704/2/1107)

Leonardi, P., Nascimbeni, V., Granata, V., & et al. 2024, *Astronomy and Astrophysics*, 686, A84, doi: [10.1051/0004-6361/202348363](https://doi.org/10.1051/0004-6361/202348363)

Levine, W. G., Vissapragada, S., Feinstein, A. D., & et al. 2024, *The Astronomical Journal*, 168, 65, doi: [10.3847/1538-3881/ad5354](https://doi.org/10.3847/1538-3881/ad5354)

Linssen, D., Oklopčić, A., & MacLeod, M. 2025, *Astronomy and Astrophysics*, 698, A112, doi: [10.1051/0004-6361/202452431](https://doi.org/10.1051/0004-6361/202452431)

Linssen, D., Shih, J., MacLeod, M., & Oklopčić, A. 2024, *Astronomy and Astrophysics*, 688, A43, doi: [10.1051/0004-6361/202450240](https://doi.org/10.1051/0004-6361/202450240)

Linssen, D. C., Oklopčić, A., & MacLeod, M. 2022, *Astronomy and Astrophysics*, 667, A54, doi: [10.1051/0004-6361/202243830](https://doi.org/10.1051/0004-6361/202243830)

Luger, R., Agol, E., Foreman-Mackey, D., & et al. 2019, *The Astronomical Journal*, 157, 64, doi: [10.3847/1538-3881/aae8e5](https://doi.org/10.3847/1538-3881/aae8e5)

Ma, L., & Fuller, J. 2021, *The Astrophysical Journal*, 918, 16, doi: [10.3847/1538-4357/ac088e](https://doi.org/10.3847/1538-4357/ac088e)

Maciejewski, G., Dimitrov, D., Fernández, M., & et al. 2016, *Astronomy and Astrophysics*, 588, L6, doi: [10.1051/0004-6361/201628312](https://doi.org/10.1051/0004-6361/201628312)

MacLeod, M., Oklopčić, A., Nail, F., & Linssen, D. 2025, *The Astrophysical Journal*, 988, 63, doi: [10.3847/1538-4357/ade0b7](https://doi.org/10.3847/1538-4357/ade0b7)

Moutou, C., Díaz, R. F., Udry, S., & et al. 2011, *Astronomy and Astrophysics*, 533, A113, doi: [10.1051/0004-6361/201116760](https://doi.org/10.1051/0004-6361/201116760)

Mukherjee, S., Sing, D. K., Fu, G., et al. 2025, arXiv e-prints, arXiv:2505.10910, doi: [10.48550/arXiv.2505.10910](https://doi.org/10.48550/arXiv.2505.10910)

NASA Exoplanet Archive. 2024,, Version: 2024-01-23 12:42 NExScI-Caltech/IPAC, doi: [10.26133/NEA12](https://doi.org/10.26133/NEA12)

Neveu-VanMalle, M., Queloz, D., Anderson, D. R., et al. 2014, *A&A*, 572, A49, doi: [10.1051/0004-6361/201424744](https://doi.org/10.1051/0004-6361/201424744)

Ngo, H., Knutson, H. A., Hinkley, S., et al. 2015, *ApJ*, 800, 138, doi: [10.1088/0004-637X/800/2/138](https://doi.org/10.1088/0004-637X/800/2/138)

Ngo, H., Knutson, H. A., Hinkley, S., et al. 2016, *ApJ*, 827, 8, doi: [10.3847/0004-637X/827/1/8](https://doi.org/10.3847/0004-637X/827/1/8)

Nichols, J. D., Wynn, G. A., Goad, M., & et al. 2015, *The Astrophysical Journal*, 803, 9, doi: [10.1088/0004-637X/803/1/9](https://doi.org/10.1088/0004-637X/803/1/9)

Oklopčić, A. 2019, *The Astrophysical Journal*, 881, 133, doi: [10.3847/1538-4357/ab2f7f](https://doi.org/10.3847/1538-4357/ab2f7f)

Oklopčić, A., & Hirata, C. M. 2018, *The Astrophysical Journal*, 855, L11, doi: [10.3847/2041-8213/aaada9](https://doi.org/10.3847/2041-8213/aaada9)

Orell-Miquel, J., Sampson, K., Morley, C. V., et al. 2025, arXiv e-prints, arXiv:2509.06847, <https://arxiv.org/abs/2509.06847>

Owen, J. E. 2019, Annual Review of Earth and Planetary Sciences, 47, 67, doi: [10.1146/annurev-earth-053018-060246](https://doi.org/10.1146/annurev-earth-053018-060246)

Owen, J. E., & Lai, D. 2018, Monthly Notices of the Royal Astronomical Society, 479, 5012, doi: [10.1093/mnras/sty1760](https://doi.org/10.1093/mnras/sty1760)

Pai Asnodkar, A., Wang, J., Broome, M., et al. 2024, MNRAS, 535, 1829, doi: [10.1093/mnras/stae2441](https://doi.org/10.1093/mnras/stae2441)

Paragas, K., Vissapragada, S., Knutson, H. A., & et al. 2021, The Astrophysical Journal, 909, L10, doi: [10.3847/2041-8213/abe706](https://doi.org/10.3847/2041-8213/abe706)

Parviainen, H., & Aigrain, S. 2015, Monthly Notices of the Royal Astronomical Society, 453, 3821, doi: [10.1093/mnras/stv1857](https://doi.org/10.1093/mnras/stv1857)

Patel, J. A., & Espinoza, N. 2022, The Astronomical Journal, 163, 228, doi: [10.3847/1538-3881/ac5f55](https://doi.org/10.3847/1538-3881/ac5f55)

Patra, K. C., Winn, J. N., Holman, M. J., & et al. 2017, The Astronomical Journal, 154, 4, doi: [10.3847/1538-3881/aa6d75](https://doi.org/10.3847/1538-3881/aa6d75)

Pérez-González, J., Greklek-McKeon, M., Vissapragada, S., & et al. 2024, The Astronomical Journal, 167, 214, doi: [10.3847/1538-3881/ad34b6](https://doi.org/10.3847/1538-3881/ad34b6)

Petrovich, C. 2015, The Astrophysical Journal, 799, 27, doi: [10.1088/0004-637X/799/1/27](https://doi.org/10.1088/0004-637X/799/1/27)

Rogers, J. G., Owen, J. E., & Schlichting, H. E. 2024, MNRAS, 529, 2716, doi: [10.1093/mnras/stae563](https://doi.org/10.1093/mnras/stae563)

Saidel, M., Vissapragada, S., Spake, J., & et al. 2025, The Astronomical Journal, 169, 104, doi: [10.3847/1538-3881/ada49f](https://doi.org/10.3847/1538-3881/ada49f)

Salvatier, J., Wiecki, T. V., & Fonnesbeck, C. 2016,, Astrophysics Source Code Library, record ascl:1610.016

Salz, M., Czesla, S., Schneider, P. C., & Schmitt, J. H. M. M. 2016, Astronomy and Astrophysics, 586, A75, doi: [10.1051/0004-6361/201526109](https://doi.org/10.1051/0004-6361/201526109)

Sanz-Forcada, J., López-Puertas, M., Lampón, M., et al. 2025, A&A, 693, A285, doi: [10.1051/0004-6361/202451680](https://doi.org/10.1051/0004-6361/202451680)

Schreyer, E., & Murray-Clay, R. 2025, submitted to the Monthly Notices of the Royal Astronomical Society

Schulik, M., & Owen, J. E. 2025, Monthly Notices of the Royal Astronomical Society, 542, 927, doi: [10.1093/mnras/staf775](https://doi.org/10.1093/mnras/staf775)

Schwarz, G. 1978, Annals of Statistics, 6, 461

Shimura, T., Mitsuishi, I., Kunitomo, M., & et al. 2025, arXiv e-prints, arXiv:2509.18677, doi: [10.48550/arXiv.2509.18677](https://doi.org/10.48550/arXiv.2509.18677)

Spake, J. J., Oklopcić, A., & Hillenbrand, L. A. 2021, The Astronomical Journal, 162, 284, doi: [10.3847/1538-3881/ac178a](https://doi.org/10.3847/1538-3881/ac178a)

Stassun, K. G., Collins, K. A., & Gaudi, B. S. 2017, The Astronomical Journal, 153, 136, doi: [10.3847/1538-3881/aa5df3](https://doi.org/10.3847/1538-3881/aa5df3)

Stefansson, G., Mahadevan, S., Hebb, L., & et al. 2017, The Astrophysical Journal, 848, 9, doi: [10.3847/1538-4357/aa88aa](https://doi.org/10.3847/1538-4357/aa88aa)

Storch, N. I., Lai, D., & Anderson, K. R. 2017, Monthly Notices of the Royal Astronomical Society, 465, 3927, doi: [10.1093/mnras/stw3018](https://doi.org/10.1093/mnras/stw3018)

Tabernero, H. M., Zapatero Osorio, M. R., Allende Prieto, C., & et al. 2022, Monthly Notices of the Royal Astronomical Society, 515, 1247, doi: [10.1093/mnras/stac1759](https://doi.org/10.1093/mnras/stac1759)

Temple, L. Y., Hellier, C., Anderson, D. R., & et al. 2019, Monthly Notices of the Royal Astronomical Society, 490, 2467, doi: [10.1093/mnras/stz2632](https://doi.org/10.1093/mnras/stz2632)

Turner, J. D., Pearson, K. A., Biddle, L. I., et al. 2016, MNRAS, 459, 789, doi: [10.1093/mnras/stw574](https://doi.org/10.1093/mnras/stw574)

Vissapragada, S., Greklek-McKeon, M., Linssen, D., & et al. 2024, The Astronomical Journal, 167, 199, doi: [10.3847/1538-3881/ad3241](https://doi.org/10.3847/1538-3881/ad3241)

Vissapragada, S., Jontof-Hutter, D., Shporer, A., & et al. 2020a, The Astronomical Journal, 159, 108, doi: [10.3847/1538-3881/ab65c8](https://doi.org/10.3847/1538-3881/ab65c8)

Vissapragada, S., Knutson, H. A., Greklek-McKeon, M., & et al. 2022, The Astronomical Journal, 164, 234, doi: [10.3847/1538-3881/ac92f2](https://doi.org/10.3847/1538-3881/ac92f2)

Vissapragada, S., Knutson, H. A., Jovanovic, N., & et al. 2020b, The Astronomical Journal, 159, 278, doi: [10.3847/1538-3881/ab8e34](https://doi.org/10.3847/1538-3881/ab8e34)

Wang, Y. H., Wang, S., Hinse, T. C., & et al. 2019, The Astronomical Journal, 157, 82, doi: [10.3847/1538-3881/aaf6b6](https://doi.org/10.3847/1538-3881/aaf6b6)

Weinberg, N. N., Sun, M., Arras, P., & Essick, R. 2017, The Astrophysical Journal, 849, L11, doi: [10.3847/2041-8213/aa9113](https://doi.org/10.3847/2041-8213/aa9113)

Wyttenbach, A., Mollière, P., Ehrenreich, D., et al. 2020, A&A, 638, A87, doi: [10.1051/0004-6361/201937316](https://doi.org/10.1051/0004-6361/201937316)

Yalçınkaya, S., Esmer, E. M., Baştürk, Ö., & et al. 2024, Monthly Notices of the Royal Astronomical Society, 530, 2475, doi: [10.1093/mnras/stae854](https://doi.org/10.1093/mnras/stae854)

Yan, D., Guo, J., Huang, C., & Xing, L. 2021, ApJL, 907, L47, doi: [10.3847/2041-8213/abda41](https://doi.org/10.3847/2041-8213/abda41)

Yan, D., Guo, J., Seon, K.-i., et al. 2024, A&A, 686, A208, doi: [10.1051/0004-6361/202348210](https://doi.org/10.1051/0004-6361/202348210)

Yan, D., Seon, K.-i., Guo, J., Chen, G., & Li, L. 2022, ApJ, 936, 177, doi: [10.3847/1538-4357/ac8793](https://doi.org/10.3847/1538-4357/ac8793)

Yan, F., & Henning, T. 2018, Nature Astronomy, 2, 714, doi: [10.1038/s41550-018-0503-3](https://doi.org/10.1038/s41550-018-0503-3)

Yee, S. W., Winn, J. N., Knutson, H. A., & et al. 2020, The Astrophysical Journal, 888, L5,
doi: [10.3847/2041-8213/ab5c16](https://doi.org/10.3847/2041-8213/ab5c16)

Youngblood, A., France, K., & et al. 2017, The Astrophysical Journal, 843, 31,
doi: [10.3847/1538-4357/aa76dd](https://doi.org/10.3847/1538-4357/aa76dd)

Zhang, Z., Morley, C. V., Gully-Santiago, M., & et al. 2023, Science Advances, 9, eadf8736,
doi: [10.1126/sciadv.adf8736](https://doi.org/10.1126/sciadv.adf8736)

Zhou, G., Bakos, G. Á., Hartman, J. D., & et al. 2017, The Astronomical Journal, 153, 211,
doi: [10.3847/1538-3881/aa674a](https://doi.org/10.3847/1538-3881/aa674a)

Zhou, G., Latham, D. W., Bieryla, A., & et al. 2016, Monthly Notices of the Royal Astronomical Society, 460, 3376, doi: [10.1093/mnras/stw1107](https://doi.org/10.1093/mnras/stw1107)